

A Systematic Study of the Short-Term X-ray Variability of Seyfert Galaxies

I. Diversity of the X-ray Rms Spectra

JINGWEI HU,^{1,2} CHICHUAN JIN,^{1,2} HUAQING CHENG,¹ AND WEIMIN YUAN^{1,2}

¹*Key Laboratory of Space Astronomy and Technology, National Astronomical Observatories, Chinese Academy of Sciences, Beijing, 100101, People's Republic of China*

²*School of Astronomy and Space Sciences, University of Chinese Academy of Sciences, 19A Yuquan Road, Beijing, 100049, People's Republic of China*

ABSTRACT

The X-ray variability of active galactic nuclei (AGN) carries crucial information about the X-ray radiation mechanism. We performed a systematic study of the X-ray short-term (1–100 ks timescale) variability for a large sample of 78 Seyferts with 426 deep *XMM-Newton* observations. In this paper, we present the time-averaged spectra and rms spectra for the entire sample, which show a variety of properties. Based on the spectral shape, we divide the rms spectra into five subtypes and the time-averaged spectra into four subtypes. The most common shape of the rms spectra is concave-down where the rms peaks at ~ 1 keV. We find that different sources can show similar time-averaged spectra and rms spectra. However, there is no one-to-one mapping between the subtypes of the time-averaged spectra and rms spectra, as similar time-averaged spectra can be accompanied by different rms spectra, and vice versa. This is likely because different physical mechanisms can produce similar rms spectra. For every subtype of the time-averaged spectra, we report its preferred subtypes of the rms spectra in both low- and high-frequency bands. We also compare the statistical properties for different subtypes, such as the black hole mass and Eddington ratio. Finally, we investigate the rms in the Fe K α line regime and find that those with a broad and extended red-wing profile tend to show stronger variability than those showing a narrow or relatively symmetric profile. Our results demonstrate the necessity of performing joint spectral and variability modeling in order to understand the mechanism of the X-ray emission in AGN. All of the rms spectra have been made publicly available.

Keywords: black hole physics - galaxies: active - X-rays: galaxies.

1. INTRODUCTION

Active galactic nuclei (AGN) are powered by the accretion of materials onto supermassive black holes (SMBHs) lying in the center of galaxies. AGN are powerful radiation sources in the universe, whose X-ray emission is believed to originate from high-energy processes in the vicinity of SMBH, such as the inverse Compton scattering in a high-temperature optically thin corona (e.g. Haardt & Maraschi 1991). Other components or processes that complicate the X-ray emission include a separate warm corona (e.g. Laor et al. 1997; Magdziarz et al. 1998; Done et al. 2012), reflection by the accretion disk or distant materi-

als (e.g. Miniutti & Fabian 2004; Ross & Fabian 2005; Fabian et al. 2013), absorption by the partially ionized/neutral gas (e.g. Turner et al. 2007; Miller 2007; Tatum et al. 2012), contribution from the galaxy (e.g. thermal plasma emission associated with star formation; Fabbiano 1989; Ranalli et al. 2003) and emission by the ionized gas on large scale (e.g. Kosec et al. 2018; Parker et al. 2021). In order to explore the X-ray mechanism of AGN, detailed modeling of their time-averaged spectra is often conducted. However, it is found that different models can provide similarly well fits to the same time-averaged spectrum and are thus degenerate. For instance, the origin of the soft X-ray excess is a matter of long debate, as it can be well fitted by both the ionized reflection model (e.g. Ross & Fabian 2005; Crummy et al. 2006; Kara et al. 2013; Fabian et al. 2013) and the warm Comptoniza-

tion model (e.g. Laor et al. 1997; Magdziarz et al. 1998; Done et al. 2012).

In order to break the model degeneracy and uncover the underlying physics of the X-ray emission, it is necessary to also take the X-ray variability into consideration. A commonly used quantity to measure the intensity of X-ray variability is the fractional root-mean-square (rms), F_{var} , which is defined as the square root of the excess variance (Edelson et al. 2002; Markowitz et al. 2003; Vaughan et al. 2003). In the frequency domain, the excess variance can be calculated by integrating the power spectral density over a range of frequencies with the Poisson noise power subtracted (Vaughan et al. 2003; Poutanen et al. 2008; Uttley et al. 2014). It is also possible to derive F_{var} for the light curves in different energy bands. Therefore, F_{var} can be measured both in a given energy band and for a given frequency range (e.g. timescale), and it is also model-independent. The frequency-differentiated rms spectra can complement the time-averaged spectral analysis and help distinguishing different spectral components (e.g. Middleton et al. 2011; Jin et al. 2013, 2017a; Parker et al. 2020; Jin et al. 2021; Härer et al. 2021).

Previous studies focusing on individual Seyferts have shown a variety of X-ray rms spectra. For example, Fabian et al. (2002) presented a long hard look at the Seyfert 1 galaxy MCG-6-30-15 with *XMM-Newton* and confirmed the presence of the broad asymmetric Fe line profile. They found that the rms spectrum show less variability at low and high energy, and the Fe line is not as variable as the continuum. This concave-down shape of the rms spectrum peaking at 1-2 keV was also observed in some other Seyferts (e.g. Vaughan & Fabian 2004; Markowitz et al. 2007), which can be interpreted as the constant soft excess and Compton reflection components plus the variable power-law component (e.g. Taylor et al. 2003). Middleton et al. (2011) performed a detailed variability analysis for RE J1034+396 and found the rms spectrum rising smoothly with energy (also see Jin et al. 2021). A similar shape of the rms spectrum was also found in the super-Eddington NLS1 RX J0136.9-3510 (Jin et al. 2009).

The shape of the rms spectrum also depends on the variability timescale (i.e. frequency band; e.g. Arévalo et al. 2008; Middleton et al. 2009). Jin et al. (2013) presented a detailed spectral-timing analysis for PG 1244+026 using a 120 ks *XMM-Newton* observation. They found at low frequencies ($8 \times 10^{-6} - 1 \times 10^{-4}$ Hz) that the soft X-rays were more variable than the hard X-rays, while the opposite was true at high frequencies ($2 \times 10^{-4} - 5 \times 10^{-3}$ Hz). There may exist several X-ray components with different variability properties and

dominating different energy bands. Alternatively, the variable component can change its spectral shape at different time scales. De Marco et al. (2020) reported on an X-ray spectral-timing analysis for NGC 3783 and detected a mildly decreasing and concave-down trend of the rms spectra in two epochs. They suggested that the change in the rms spectrum is due to incoherent fast variability of X-ray obscuration on timescales between about 1 hour to 10 hours. Parker et al. (2021) reported the different rms spectra of the NLS1 1H 0707-495 in different frequency bands and modeled them with variability introduced by both reflection and absorption.

While previous works have shown that the rms spectrum is useful for studying the X-ray mechanism, they are mostly limited to individual sources. The main objective of this work is to obtain a systematic understanding of the diversity of the X-ray rms spectra of Seyferts, and look for potential connections between the rms spectra and time-averaged spectra. To achieve this objective, we collect a large sample of 78 Seyferts showing significant short-term X-ray variability (1-100 ks timescales) and use 426 archival *XMM-Newton* observations to measure the time-averaged spectra and rms spectra in different frequency bands for all the sources.

This paper is organized as follows. In Section 2, we introduce the selection criteria and statistical properties of the sample and the data analysis procedures. In Section 3, we present a statistical view of the diversity of rms spectra for the entire sample. This is followed by Section 4, which presents various systematic connections between the time-averaged spectra and rms spectra. The variability analysis of Fe $K\alpha$ is presented in Section 5. Further discussions about the diverse rms spectra and the variation in the rms spectrum between different observations of individual sources are provided in Section 6. The final section summarizes all the main results of this work.

2. SAMPLE SELECTION AND DATA REDUCTION

2.1. Sample Selection

We first adopt the sample of 43 Seyfert galaxies from Kara et al. (2016), in which the authors performed a global look at their X-ray time lags. The sample included Seyferts observed with the *XMM-Newton* (Jansen et al. 2001) up to 2015 January 1, with continuous observations longer than 40 ks. By using the same selection criterion, Seyferts with observations publicly available between 2015 January 1 and 2020 January 1 are also added into our sample. Furthermore, for all the selected sources, we use all the *XMM-Newton* observations longer than 10 ks. This results in a large sample of 78 Seyfert galaxies with a total of 426 *XMM-Newton*

observations. We note that our Seyfert sample contains six radio-loud sources with 18 observations and is thus dominated by radio-quiet objects.

To characterize our sample, we compiled the black hole masses of these AGN from the literature. We prioritize the black hole mass M_{BH} measured by reverberation mapping and then by other methods, such as the relations for the stellar velocity dispersion and the narrow-line region, as well as virial masses measured from the broad-line region. The redshifts, R.A., and decl. coordinates are taken from NED¹. The Galactic absorption column densities $N_{\text{H,gal}}$ toward the line of sight are taken from HI4PI Collaboration et al. (2016). The Eddington ratio (λ_{Edd}) is taken from the literature (e.g. Vasudevan & Fabian 2009; Vasudevan et al. 2009).

All the parameters mentioned above are listed in Table 1 for every source. The distributions of the redshift, black hole mass, Eddington ratio, good time interval (GTI), 0.3-10 keV net photon counts, and 0.3-10 keV luminosity of the selected sample are plotted in Figure 1. It shows that the majority (87%) of the sample lies below redshift 0.1. More than half of the total observations have GTI longer than 40 ks. The median values for the 0.3-10 keV net photon counts and the 0.3-10 keV luminosity are derived to be 2×10^5 and $3 \times 10^{43} \text{erg s}^{-2}$, respectively.

2.2. Data Reduction

In order to study the X-ray spectra and variability, we use the data from the *XMM-Newton* EPIC-pn camera as it provides the highest source count rate. The observation data files (ODF) of each observation are retrieved from the *XMM-Newton* Science Archive (XSA)². Then the data are reduced and analyzed using the *XMM-Newton* Science Analysis Software (SAS v16.0.0)³.

Following the SAS data analysis threads, the `epproc` (for EPIC-pn) task is used to reprocess the data and generate new event lists. For observations with more than one calibrated and concatenated event lists of EPIC-pn, we select all useful segments to generate scientific products. We adopt a typical circular source extraction region of 40'' radius centered at the source coordinates. The background is determined from a nearby source-free region, which is 50'' radius in the *PrimeSmallWindow* mode and 80'' radius in larger window modes. The effect of background flares are taken into account, because it may affect the analysis of variability. To do this, we visually check every background light curve and filter

the event lists with the `tabgtigen` task to remove time intervals where background flares are severe. For the purpose of reliable timing analysis, we only use continuous GTIs of more than 10 ks long (Figure 1(d)).

For the EPIC-pn camera, $\sim 66.9\%$ of the observations were operated in the *PrimeSmallWindow* mode, while the others were in the *PrimeFullWindow* mode ($\sim 14.3\%$), the *PrimeFullWindowExtended* mode ($\sim 0.5\%$) and the *PrimeLargeWindow* mode ($\sim 18.3\%$), thus photon pileup can be a problem for bright sources. Therefore, we check the pileup effect by running the `epatplot` task and minimize it by excising the core of the point spread function (PSF) in case of need, i.e. replacing the circular region with an annular region.

Within the selected GTIs, both light curves and time-averaged X-ray spectra are extracted from the source and background regions with the `evselect` task. Only good events with `PATTERN` ≤ 4 are adopted for analysis. The light curves are binned with 100 s per bin. The background-subtracted source light curves are produced with the `epiclccorr` task. The redistribution matrix and ancillary file are produced for each spectrum with the SAS tasks `rmfgen` and `arfgen`. All the spectra are rebinned with the FTOOLS task `grppha`, so that each bin contains at least 25 counts. XSPEC v12.9.1 is used to perform all the spectral fitting.

In order to measure the optical/UV flux of each source in every observation, we also reduce all the data from the *XMM-Newton* Optical Monitor (OM). The OM data are reprocessed with the `omichain` task.

The rms variability amplitude from X-ray light curves is calculated by adopting the frequency-resolved spectral techniques. The calculation procedure is summarized in Appendix A.1 (see also Vaughan et al. 2003; Arévalo et al. 2008; Poutanen et al. 2008; Jin et al. 2017a). We emphasize that the subtraction of the Poisson noise power can affect the accuracy of the rms significantly. We find that the theoretical Poisson noise power can significantly underestimate the true Poisson noise, which then leads to the overestimate of the intrinsic rms, and so further corrections should be applied. We suggest that the arithmetic average of the power over the power spectra density (PSD) high-frequency range, which is dominated by the Poisson noise power is the most accurate method in this work. A detailed prescription of the determination of the Poisson noise power can be found in Appendix A.2.

3. THE DIVERSE RMS AND TIME-AVERAGED SPECTRA: A STATISTIC VIEW

3.1. Production of the Rms and Time-averaged Spectra

¹ <https://ned.ipac.caltech.edu/>

² <http://nxsas.esac.esa.int>

³ <https://www.cosmos.esa.int/web/XMM-Newton/sas-threads>

Table 1. Table of the 78 sources in this sample, with a total of 426 observations

Source Name	Type	R.A.	Decl.	Redshift	$N_{\text{H-gal}}$	Number(obs)	$\log M_{\text{BH}}$	$\log \lambda_{\text{Edd}}$	References
		(J2000.0)	(J2000.0)		(10^{22} cm^{-2})		(M_{\odot})		
(1)	(2)	(3)	(4)	(5)	(6)	(7)	(8)	(9)	(10)
1ES 1927+654	Sy2	291.8313	65.5651	0.017	0.064	3	7.34	-2.23	1
1H 0323+342	NLS1 ^a	51.1715	34.1794	0.061	0.117	7	7.10	-0.40	2
1H 0419-577	Sy1.5	66.5029	-57.2003	0.104	0.012	8	8.11	-0.60	3
1H 0707-495	NLS1	107.1729	-49.5519	0.041	0.040	14	6.31	0.00	4
1H 1934-063	NLS1/Sy1.5	294.3875	-6.2180	0.010	0.102	2	7.32	-1.84	5
3C 120	Sy1.5 ^a	68.2962	5.3543	0.033	0.103	5	7.74 ^b	-0.52	6,7
3C 390.3	Sy1.5 ^a	280.5375	79.7714	0.056	0.037	2	8.46 ^b	-1.33	6,7
Ark 120	Sy1	79.0476	-0.1498	0.033	0.100	6	8.18 ^b	-0.95	6,7
Ark 564	NLS1	340.6639	29.7254	0.025	0.050	13	6.06	0.29	4
CTS A08.12	Sy1.2	323.0090	-33.7150	0.030	0.033	1	7.80	-0.60	8,9
ESO 113-G010	NLS1/Sy1.8	16.3197	-58.4373	0.026	0.020	1	6.85	-1.25	10,9
ESO 198-G24	Sy1	39.5819	-52.1924	0.045	0.027	2	8.28	-1.32	5
ESO 362-G18	Sy1.5	79.8992	-32.6576	0.012	0.013	2	7.49	-1.21	5
ESO 511-G030	Sy1	214.8434	-26.6447	0.022	0.043	1	7.84	-1.58	11
FBQS J1644+2619	NLS1 ^a	251.1771	26.3203	0.145	0.050	1	7.28	-0.79	12
Fairall 9	Sy1.2	20.9407	-58.8058	0.047	0.029	6	8.41 ^b	-1.73	6,7
HE 1029-1401	Sy1	157.9762	-14.2808	0.086	0.057	1	9.08	-1.15	13
HE 1353-1917	Sy1	209.1528	-19.5292	0.035	0.071	1	8.13	-1.93	14
IC 4329A	Sy1.2	207.3303	-30.3094	0.016	0.041	3	8.29	-1.38	11
IRAS 05078+1626	Sy1.5	77.6896	16.4988	0.018	0.189	1	7.20	-1.40	5
IRAS 13224-3809	NLS1	201.3307	-38.4146	0.066	0.048	19	6.82	0.81	4
IRAS 13349+2438	NLS1	204.3280	24.3843	0.108	0.011	4	8.62	-1.64	15
IRAS 17020+4544	NLS1	255.8766	45.6798	0.060	0.025	4	6.77	-0.17	16,17
IRAS 18325-5926	Sy2	279.2429	-59.4024	0.020	0.052	3	6.36	0.14	18
IRAS F12397+3333	NLS1	190.5441	33.2841	0.044	0.014	2	6.88 ^b	-1.08	19,12
I Zw 1	NLS1	13.3956	12.6934	0.059	0.046	10	7.20	0.11	4
MCG-02-14-009	Sy1	79.0882	-10.5615	0.028	0.101	1	7.07	-0.92	20
MCG-5-23-16	Sy1.9	146.9173	-30.9487	0.008	0.078	5	7.85	-1.14	21
MCG-6-30-15	NLS1/Sy1.5	203.9738	-34.2955	0.008	0.036	8	6.31 ^b	-0.35	22,23
MR 2251-178	Sy1.5	343.5242	-17.5819	0.064	0.026	8	8.28	-0.80	24
MS 22549-3712	NLS1	344.4127	-36.9350	0.039	0.010	2	6.58	-0.43	25
Mrk 1040	Sy1	37.0603	31.3117	0.017	0.067	3	6.36	-0.73	4
Mrk 1044	NLS1	37.5230	-8.9981	0.016	0.029	5	6.15 ^b	-0.05	26,3
Mrk 110	NLS1	141.3036	52.2863	0.016	0.013	1	7.40 ^b	-0.36	6,7

NOTE—The columns are: (1) the name of the source; (2) classification of the source, ^a marks the radio-loud sources, while the rest are radio-quiet objects; (3) R.A. coordinates in units of degree; (4) decl. coordinates in units of degree; (5) redshift of the source derived from the NASA/IPAC Extragalactic Database; (6) the Galactic absorption column density $N_{\text{H-gal}}$ toward the line of sight of each of the source in units of 10^{22} cm^{-2} ; (7) number of observations used for each source; (8) the mass of the central black hole in units of M_{\odot} ; (9) the Eddington ratio; (10) references for M_{BH} and λ_{Edd} values: (1) Tran et al. (2011); (2) León Tavares et al. (2014); (3) Grupe et al. (2010); (4) Bian & Zhao (2003); (5) Wang & Zhang (2007); (6) Peterson et al. (2004); (7) Vasudevan & Fabian (2009); (8) Busch et al. (2014); (9) Laha et al. (2018); (10) Cackett et al. (2013); (11) Vasudevan et al. (2010); (12) Liu et al. (2019); (13) Woo & Urry (2002); (14) Husemann et al. (2019); (15) Czerny et al. (2004); (16) Wang & Lu (2001); (17) Longinotti et al. (2018); (18) Iwasawa et al. (2016); (19) Du et al. (2014); (20) Williams et al. (2018); (21) Zhou & Wang (2005); (22) Bentz et al. (2016); (23) Vasudevan et al. (2009); (24) Wang et al. (2009); (25) Zhang & Wang (2006); (26) Wang et al. (2014); (27) Laor (1998); (28) Bentz et al. (2009); (29) Risaliti et al. (2009); (30) Peterson et al. (2005); (31) Denney et al. (2006); (32) Vasylenko (2018); (33) Bentz et al. (2014); (34) Pancoast et al. (2014); (35) Jin et al. (2012); (36) Lewis & Eracleous (2006); (37) Gliozzi et al. (2010); (38) Jin et al. (2009); (39) Malizia et al. (2008).

^b M_{BH} was measured through reverberation mapping, based on equation $M_{\text{BH}} = f \frac{c r v^2}{G}$ with an adopted mean value $\langle f \rangle = 5.5$. The rest of M_{BH} were estimated from other methods.

Table 1. -continued

Source Name	Type	R.A. (J2000.0)	Decl. (J2000.0)	Redshift	$N_{\text{H-gal}}$ (10^{22} cm^{-2})	Number(obs)	$\log M_{\text{BH}}$ (M_{\odot})	$\log \lambda_{\text{Edd}}$	References
(1)	(2)	(3)	(4)	(5)	(6)	(7)	(8)	(9)	(10)
Mrk 205	Sy1	185.4343	75.3108	0.071	0.029	6	8.68	-1.23	15
Mrk 279	Sy1	208.2644	69.3082	0.030	0.013	4	7.54 ^b	-0.67	6,7
Mrk 335	NLS1	1.5813	20.2029	0.026	0.033	8	7.15 ^b	-0.08	6,7
Mrk 478	NLS1	220.5310	35.4397	0.079	0.009	5	7.43	-0.82	3
Mrk 493	NLS1	239.7899	35.0297	0.031	0.020	2	6.18 ^b	-0.06	26,3
Mrk 509	Sy1.5	311.0406	-10.7235	0.034	0.039	15	8.16 ^b	-1.02	6,7
Mrk 586	Sy1.2	31.9578	2.7154	0.156	0.028	1	7.55	0.76	27
Mrk 590	Sy1	33.6398	-0.7667	0.026	0.028	2	7.68 ^b	-1.98	6,7
Mrk 704	Sy1.2	139.6084	16.3053	0.029	0.027	2	7.76	-0.97	5
Mrk 766	NLS1	184.6105	29.8129	0.013	0.018	9	6.25 ^b	-0.30	28,23
Mrk 841	Sy1.5	226.0050	10.4378	0.036	0.020	5	8.17	-1.67	23
NGC 1365	Sy1.8	53.4015	-36.1404	0.005	0.012	11	6.30	-0.43	29,11
NGC 1566	Sy1.5	65.0017	-54.9378	0.005	0.007	3	6.11	-1.61	5
NGC 2992	Sy1.9	146.4252	-14.3264	0.008	0.052	10	7.27	-1.70	11
NGC 3227	Sy1.5	155.8774	19.8651	0.004	0.019	9	7.63 ^b	-3.01	6,7
NGC 3516	Sy1.5	166.6979	72.5686	0.009	0.031	6	7.63 ^b	-2.21	6,7
NGC 3783	Sy1.5	174.7573	-37.7387	0.010	0.101	6	7.47 ^b	-1.40	6,7
NGC 4051	NLS1	180.7901	44.5313	0.002	0.012	19	6.28 ^b	-1.80	6,7
NGC 4151	Sy1.5	182.6357	39.4057	0.003	0.021	18	7.12 ^b	-1.16	6,7
NGC 4395	Sy1.8	186.4536	33.5469	0.001	0.043	4	5.56 ^b	-2.92	30
NGC 4593	Sy1	189.9143	-5.3443	0.009	0.017	8	6.99 ^b	-1.43	31,7
NGC 4748	NLS1	193.0519	-13.4147	0.015	0.036	1	6.41 ^b	-0.14	28,32
NGC 5273	Sy1.9	205.5345	35.6542	0.004	0.008	3	6.78 ^b	-2.42	33,12
NGC 5506	NLS1	213.3120	-3.2076	0.006	0.042	9	7.67	-1.56	11
NGC 5548	Sy1.5	214.4981	25.1368	0.017	0.015	19	7.83 ^b	-1.63	6,7
NGC 6814	Sy1.5	295.6692	-10.3235	0.005	0.085	2	7.27 ^b	-2.43	28,34
NGC 6860	Sy1.5	302.1954	-61.1002	0.015	0.030	1	7.91	-2.07	11
NGC 7213	Sy1.5	332.3180	-47.1666	0.006	0.011	2	7.37	-2.11	11
NGC 7314	Sy2	338.9425	-26.0505	0.005	0.015	5	6.14	-1.28	11
NGC 7469	Sy1.5	345.8151	8.8740	0.016	0.045	11	7.09 ^b	-0.43	6,7
NGC 985	Sy1.5	38.6574	-8.7876	0.043	0.035	5	8.36	-1.69	23
PG 1211+143	NLS1	183.5736	14.0536	0.081	0.026	11	8.16 ^b	-0.62	6,7
PG 1244+026	NLS1	191.6469	2.3691	0.048	0.017	6	6.79	0.58	35
PG 1448+273	NLS1	222.7865	27.1574	0.065	0.030	3	7.26	0.46	35
Pictor A	Sy1 ^a	79.9572	-45.7788	0.035	0.036	2	7.60	-0.96	36
PKS 0558-504	NLS1	89.9474	-50.4479	0.137	0.033	15	8.40	0.23	37
PKS J1220+0203	Sy1.2 ^a	185.0495	2.0617	0.240	0.018	1	8.84	-0.92	12
RBS 229	Sy1.2	25.0708	-0.8342	0.334	0.027	1	9.01	-1.10	12
RE J1034+396	NLS1	158.6608	39.6412	0.042	0.013	8	6.23	0.67	35
RX J0136.9-3510	NLS1	24.2267	-35.1644	0.289	0.017	1	7.89	0.43	38
RX J0439.6-5311	NLS1	69.9112	-53.1919	0.243	0.006	2	6.59	1.11	3
SWIFT J2127.4+5654	NLS1	321.9373	56.9444	0.014	0.729	5	7.18	-0.40	39
TON S180	NLS1	14.3342	-22.3823	0.062	0.013	4	6.85	0.80	3
Ton 28	Sy1	151.0109	28.9265	0.327	0.018	1	8.00	-0.27	12

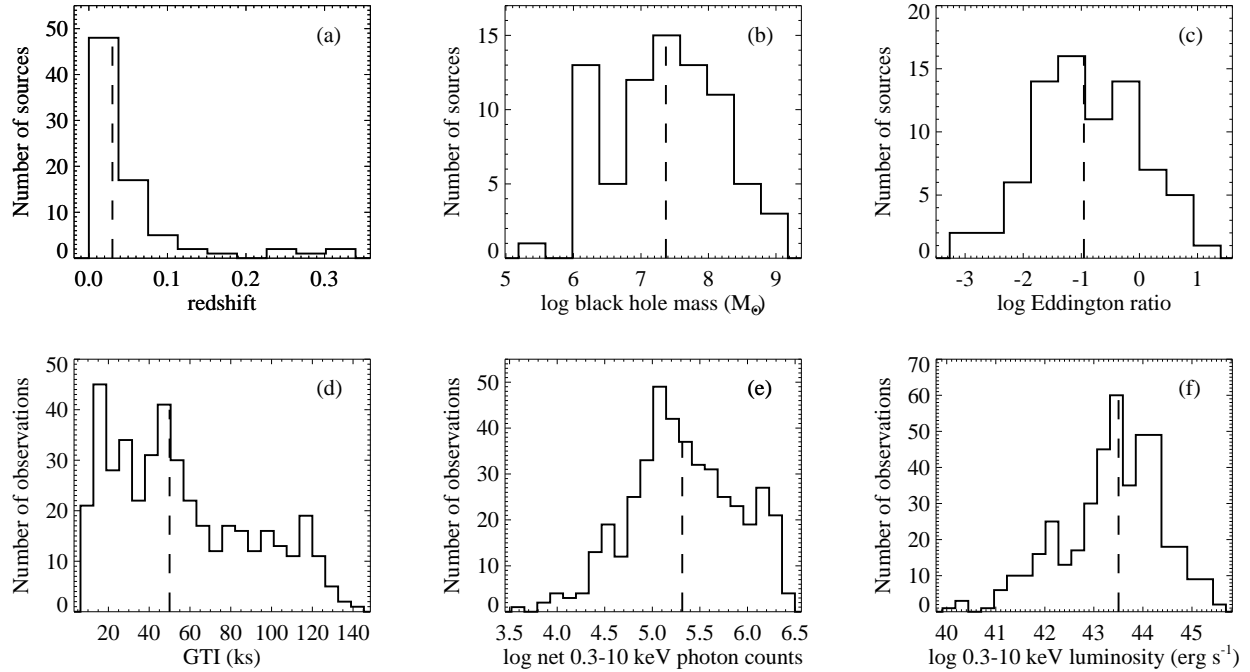


Figure 1. Distributions of different properties in our sample. The dashed line denotes the median. (a) Distribution of the redshift of the sample objects. (b) Distribution of the black hole mass. (c) Distribution of the Eddington ratio. (d) Distribution of the GTI of each observation. (e) Distribution of the 0.3-10 keV net photon counts. (f) Distribution of the 0.3-10 keV luminosity.

A time-averaged spectrum shows the source flux in every energy bin. In comparison, an rms spectrum shows fractional flux variation in every energy bin (see Uttley et al. 2014 and references therein). The amplitude of variation is also dependent on the variation frequency (i.e. timescale; Jin et al. 2013, 2017a). Therefore, a joint analysis of the time-averaged spectrum and rms spectrum will allow the exploration of different spectral components with different variability properties.

We calculate the rms spectra for the entire sample of 78 Seyfert galaxies and 426 *XMM-Newton* observations. In order to increase the accuracy of rms measurement, we adopt a careful selection of seven energy bins spanning 0.3-10 keV, in order to keep sufficient photon counts per bin and to produce reliable power spectra. These energy bins are selected to reach a reasonable compromise between the spectral resolution and the accuracy of rms measurement in every energy bin. In some cases the source flux is still too low to produce reliable rms in individual energy bins, then we merge adjacent bins to increase the count rates, at the expense of losing more energy resolution. On the other hand, for a subset of bright sources, the energy resolution of the rms spectra can be increased to allow a more detailed study. However, for the consistency of rms spectra production and ease of shape comparison for the entire sample, we

do not optimize the energy resolution for every source. These bright sources can be investigated in more detail on a case by case basis (e.g. Parker et al. 2020; Härer et al. 2021).

In addition, we divide the frequency range into the low-frequency (LF; $< 10^{-4}$ Hz) and high-frequency (HF; $10^{-4} - 10^{-3}$ Hz) bands, in order to explore the frequency (i.e. timescale) dependence of the rms spectra. To this end, observations without complete fractional LF or HF rms spectra across 0.3-10 keV (due to unconstrained rms in some energy bins) are discarded, while those with high-quality rms spectra are culled, including 330 observations of 69 sources.

For each of these sources, we extract the time-averaged spectrum in every observation. Then these 330 time-averaged spectra are fitted in 2-10 keV with a single power-law model absorbed by a Galactic column and a free intrinsic column. The absorption is modeled by the (z)TBabs model (Wilms et al. 2000), and the Galactic column is fixed at the value along the source’s line of sight (HI4PI Collaboration et al. 2016). Then we produce the unfolded time-averaged spectra for the following analysis.

3.2. A Typical Example: Mrk 766

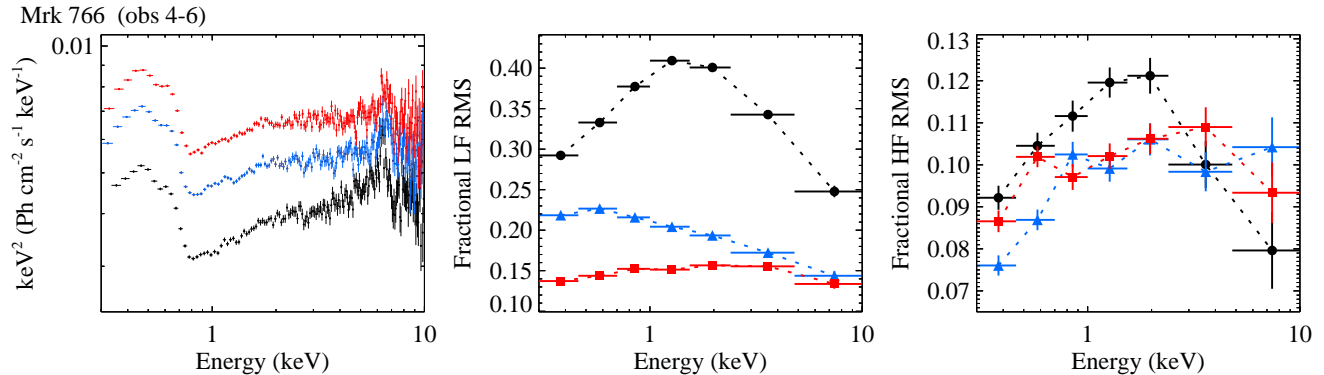


Figure 2. Typical example of the results of the connection of the rms spectra with the time-averaged spectra for the case of Mrk 766. Similar plots for other sources in Table 1 can be found in the appendix. The left panel shows the unfolded time-averaged spectra of three separate observations. The middle panel shows the fractional rms of each individual observation in the low frequency (LF; $< 10^{-4}$ Hz). The right panel shows the fractional rms in the high frequency (HF; $10^{-4} - 10^{-3}$ Hz).

Firstly, we show a typical example from the above analysis, which is Mrk 766 shown in Figure 2. The unfolded time-averaged spectra from three separate observations are shown in the left panel. These observations were conducted between 2005 May 25 and 2005 May 29. These spectra mainly differ in their overall fluxes, while their shapes are all similar, including a power-law-shape continuum above 2 keV, a significant Fe $K\alpha$ emission line in 6-7 keV and a strong soft X-ray excess below 0.8 keV.

The fractional rms spectra of each individual observation in LF and HF are shown in the middle and right panel, respectively. The LF rms spectra show various spectral shapes in different observations. The concave-down shape of the LF rms spectrum in black indicates that the soft excess and the hard X-ray component are much less variable than the middle energy band of 1-2 keV. This can be qualitatively explained by the classic disk-reflection model (e.g. Miniutti & Fabian 2004; Ross & Fabian 2005; Fabian et al. 2013), where the soft excess and hard X-ray is dominated by the relatively constant reflection component, while the more variable primary power law dominates the energy band in the middle. Parker et al. (2020) presented simple XSPEC models for fitting the excess variance spectra and found that the rms spectra of IRAS 13224-3809 can be well described by a variable power law damped with a constant soft excess and a less-variable relativistic reflection component, enhanced with a ultrafast outflow (UFO) in that case. Alternatively, this can also be qualitatively explained by the ionized absorption model, where the variability of the ionized absorption introduces a peak of the rms in the energy band round 1 keV (Parker et al. 2021).

However, Figure 2 also shows that the situation is much more complicated. We see that as the flux of the

time-averaged spectra increases, the overall LF rms decreases. This can be understood as if there is a constant component contributing more flux to the higher-flux time-averaged spectra across the entire 0.3-10 keV. However, then we also observe a significant change in the shape of the LF rms spectra as the flux increases, which is difficult to explain in the reflection scenario. Another possibility is that the low-flux spectrum is more absorbed and the absorber can introduce short-term variability (Gardner & Done 2014), but this also requires more detailed quantitative analysis of all the observations of Mrk 766, which is beyond the scope of this work. On the other hand, the HF fractional rms spectra are roughly similar, which mainly follow the concave-down shape.

A linear relation between the rms variability and flux was observed in X-ray binaries (XRBs) and AGN (Uttley & McHardy 2001; Gaskell 2004), suggesting that variations on different timescales must be coupled together (Uttley et al. 2005). For each observation of Mrk 766 in our sample, we also find a linear relation between the average absolute rms amplitude and the flux on short timescales. This is consistent with previous results by using 2001 *XMM-Newton* data (Vaughan et al. 2003) and 2005 *XMM-Newton* data (Markowitz et al. 2007). We also explore this relation on long timescales. Although three observations shown in Figure 2 display an anticorrelation between the LF rms and flux, the total nine observations of this source exhibit a positive linear rms-flux correlation. A more complete analysis about this rms-flux relation of our sample will be presented in a following paper (Hu et al. 2022, in preparation).

The example of Mrk 766 clearly shows that there is a complex diversity in the shape of the rms spectrum, and its link to the time-averaged spectrum is also com-

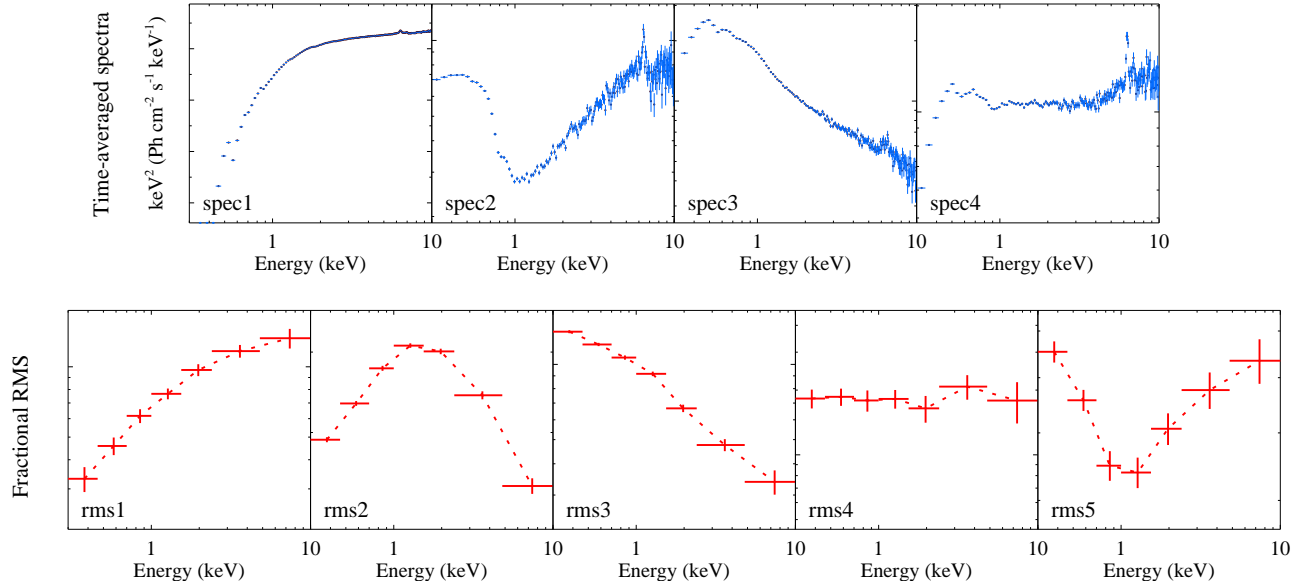


Figure 3. Type of the spectral shape of the time-averaged spectra and the fractional rms spectra. The time-averaged spectra, plotted in $E^2 N(E)$, can be classified as: (spec1) increasing with energy; (spec2) concave-up; (spec3) decreasing with energy; (spec4) flat. The LF and HF rms spectral shapes can be classified as: (rms1) increasing with energy; (rms2) concave-down; (rms3) decreasing with energy; (rms4) flat; (rms5) concave-up.

plicated. More results for other sources are shown in Figure A2 in the appendix. In order to obtain a global understanding of the diversity and complexity of the rms and time-averaged spectra, we perform a statistical analysis of these spectra using the entire sample of 69 Seyferts and 330 observations.

3.3. Statistical Results

Firstly, we visually inspect all the rms and time-averaged spectra. Then based on the observed spectral shapes, we classify the spectra into several subsamples, as shown in Figure 3. For the time-averaged spectra plotted in $E^2 N(E)$, which is unfolded through a power-law model, the spectral shapes are classified as: (spec1) increasing with energy; (spec2) concave-up; (spec3) decreasing with energy; (spec4) flat. In addition, the fractional LF and HF rms spectral shapes are classified as: (rms1) increasing with energy; (rms2) concave-down; (rms3) decreasing with energy; (rms4) flat; (rms5) concave-up. Then we calculate the mean value of some key parameters within each subsample, including the hard X-ray photon index ($\Gamma_{2-10\text{ keV}}$), black hole mass (M_{BH}), and Eddington ratio (λ_{Edd}). The results are presented in Table 2. The distributions of the photon index, black hole mass M_{BH} , and Eddington ratio λ_{Edd} for every subsample are plotted in Figs. 4 and 5. Note that one source may appear in multiple subsamples, if it shows more than one type of spectral shape in different observations.

For the time-averaged spectra, we find that the spec3 group has the steepest mean $\Gamma_{2-10\text{ keV}}$ of 2.15. Its mean λ_{Edd} of 0.575 is also the largest among the four groups. This is because many Seyferts in the spec3 group are super-Eddington NLS1s (see Figure 4), such as PG 1244+026 (Jin et al. 2013), RX J0439.6-5311 (Jin et al. 2017b), and RX J0136.9-3510 (Jin et al. 2009). This group also has the smallest mean M_{BH} , as expected for these NLS1s with $M_{\text{BH}} \lesssim 10^7 M_{\odot}$. On the contrary, the spec1 group has the smallest $\Gamma_{2-10\text{ keV}}$ of 1.40, and its mean λ_{Edd} is only 0.032. This is consistent with the known correlation found between the hard X-ray photon index and Eddington ratio in various AGN samples (e.g. Lu & Yu 1999; Wang et al. 2004; Shemmer et al. 2008; Ai et al. 2011; Trump et al. 2011; Jin et al. 2012; Qiao & Liu 2018; Cheng et al. 2019). It is also interesting to note that the spec4 group has the largest mean M_{BH} of $4.8 \times 10^7 M_{\odot}$ and small mean λ_{Edd} of 0.071.

Among the five HF rms groups, the HF rms1 group shows the largest mean $\Gamma_{2-10\text{ keV}}$ of 1.96 in their corresponding time-averaged spectra and the largest mean λ_{Edd} of 0.324. This means that sources with higher Eddington ratios tend to show stronger HF variability in the hard X-ray band. In comparison, the lowest mean λ_{Edd} of 0.091 is found in the HF rms3 group. The smallest mean $\Gamma_{2-10\text{ keV}}$ of 1.66 is found in the HF rms3 and rms5 group, both of which show increasing fractional rms toward lower energy below 1 keV.

Among the five LF rms groups, we find that the LF rms1 group shows the largest mean $\Gamma_{2-10\text{keV}}$ of 1.80 and the largest mean λ_{Edd} of 0.234, similar to the HF rms1 group. The lowest mean λ_{Edd} of 0.087 is found in the LF rms4 group. The low λ_{Edd} of the LF and HF rms4 groups indicates that sources with low Eddington ratios tend to show similar fractions of variability across the 0.3-10 keV in both the LF and HF bands.

The above results suggest the likely presence of systematic links between the rms and time-averaged spectra, which are described in the next section.

4. CONNECTIONS BETWEEN THE RMS AND TIME-AVERAGED SPECTRA

The AGN’s X-ray spectral fitting is often degenerated to different models, because a range of physical processes can affect the spectral shape. For example, multiple components can contribute to the X-ray spectrum at the same time, such as the disk blackbody emission, warm/hot corona Comptonization, neutral/ionized reflection, emission from environmental gas. Also, the spectral shape can be modified by absorbers along the line of sight with different velocities, ionization states, and covering factors. In addition, the strong gravity around the SMBH and the disk wind materials with different velocities can provide smearing mechanisms for the emission/absorption lines. Therefore, a joint analysis of the rms spectra is especially important because it can provide additional constraints on the X-ray production mechanism (e.g. Middleton et al. 2011; Jin et al. 2013; Parker et al. 2014, 2015; Jin et al. 2021; Parker et al. 2021). The large sample of AGN with high-quality data presented in this work enables us, for the first time, to explore the possible systematic links between the rms spectra and time-averaged spectra.

As shown in Table 3, for each of the time-averaged spectral groups from spec1 to spec4, we calculate the proportions of different rms spectral groups. If several observations of one source show the same type of the time-averaged spectra and the same type of the rms spectra, then they are counted only once. If a source shows one type of time-averaged spectrum but multiple types of rms spectra, then it is counted in the calculation of proportion for those types of rms spectra. To visualize the links, the distributions of different types of the time-averaged spectra within every rms spectral group are plotted in Figure 6. These table and figure show a range of systematic connections between the time-averaged spectra and rms spectra, as below.

(a) The most common rms spectral shape is rms2, where the fractional rms peaks in the energy band of 1-2 keV and decreases toward both soft and hard X-

rays. Rms2 dominates the spectral groups from spec1 to spec3. This type of rms spectral shape can be modeled with the ionized reflection model, where the middle energy band contains the highest fraction of the primary continuum emission, which is most variable (e.g. Kara et al. 2015; Parker et al. 2021). The only exception is the spec4 group, where the spectral shape is relatively flat. This group prefers a relatively flat HF rms spectrum, i.e. the HF rms4, although in the LF band this group is still dominated by the LF rms2.

(b) The rarest rms spectral shape is rms5, where both the soft and hard X-rays are more variable than the energy band of 1-2 keV. This energy band is sensitive to the emission lines which can be less variable than the continuum (e.g. Liu et al. 2021). The dip can be due to the photoionized gas emission on large scales (e.g. narrow-line region, galactic scales), and it is found that a strong damping feature around 1 keV in proper ionization can exist in the rms spectra (Parker et al. 2021), so this might explain the few cases where such an rms spectral shape is observed.

(c) The spec1 group appears most severely absorbed in the soft X-rays. Interestingly, we find that the second most preferred rms spectral shape of this group is rms4 in the HF band, which is relatively flat. This means that in 27.5% sources of this spectral group, the absorption does not increase or suppress the HF variability in the soft X-ray band. In comparison, the second most preferred rms in the LF band is rms3, which shows an enhanced fractional variability toward soft X-rays. This may suggest that either the absorption introduces extra LF variability (e.g. Parker et al. 2021), or that the spectral components with less LF variability are more strongly absorbed.

(d) The shape of the spec2 group is mainly dominated by rms2. The shapes of the time-averaged spectra and rms spectra are qualitatively consistent with both the ionized reflection model and warm absorption model. Some sources in this group has been studied in great details, such as 1H 0707-495 (e.g. Parker et al. 2021) and IRAS 13224-2809 (e.g. Parker et al. 2020; Alston et al. 2020).

(e) The shape of the spec3 group is typical for some “X-ray simple” NLS1s (Gallo 2006). We note that the second most preferred rms spectral shape of this group is rms1 in the HF band and rms3 in the LF band. These results are consistent with previous studies on some super-Eddington NLS1s such as PG 1244+026 (Jin et al. 2013) and RX J0439.6-5311 (Jin et al. 2017a), where the soft excess is dominated by a separate warm Comptonization component, which is more variable than the hard X-rays in the LF band but less variable in the HF band. In the

Table 2. Properties of the Selected Samples

Spectral shape	$N_{\text{src-all}}$	$\langle \text{Redshift} \rangle$	$\langle \Gamma_{2-10 \text{ keV}} \rangle$	$\langle F_{0.3-10 \text{ keV}} \rangle$ ($10^{-11} \text{ erg s}^{-1} \text{ cm}^{-2}$)	$\langle L_{0.3-10 \text{ keV}} \rangle$ ($10^{43} \text{ erg s}^{-1}$)	$\langle \log M_{\text{BH}} \rangle$ (M_{\odot})	$\langle \log \lambda_{\text{Edd}} \rangle$
(1)	(2)	(3)	(4)	(5)	(6)	(7)	(8)
spec1	22	0.017	1.40	4.8	2.0	7.21	-1.50
spec2	14	0.029	1.64	2.6	3.9	7.16	-1.05
spec3	26	0.073	2.15	2.3	25.3	7.05	-0.24
spec4	18	0.034	1.77	4.6	14.3	7.68	-1.15
HF rms1	22	0.056	1.96	3.2	23.6	7.30	-0.49
HF rms2	40	0.047	1.78	3.3	14.8	7.16	-0.83
HF rms3	23	0.021	1.66	3.7	4.6	7.16	-1.04
HF rms4	40	0.035	1.69	3.9	13.6	7.50	-0.97
HF rms5	18	0.033	1.66	3.9	14.0	7.28	-0.77
LF rms1	20	0.052	1.80	3.6	14.7	7.25	-0.63
LF rms2	51	0.044	1.79	3.8	15.0	7.30	-0.92
LF rms3	35	0.029	1.77	3.5	5.8	7.17	-0.93
LF rms4	12	0.038	1.75	4.0	12.7	7.58	-1.06
LF rms5	15	0.043	1.73	3.1	17.4	7.36	-0.66

NOTE—The columns are: (1) different time-averaged spectral shape and rms spectral shape (spec1~spec4, rms1~rms5); (2) total number of source, several observations of one source showing the same type of the spectral shape are classified as one source; (3) average redshift; (4) average photon index; (5) average 0.3-10 keV flux in units of $10^{-11} \text{ erg s}^{-1} \text{ cm}^{-2}$; (6) average 0.3-10 keV luminosity in units of $10^{43} \text{ erg s}^{-1}$; (7) average logarithmic black hole mass in units of M_{\odot} ; (8) average logarithmic Eddington ratio.

Table 3. Proportion of Different Subsamples

Time-averaged spectra	Fractional HF rms Spectra						Fractional LF rms Spectra					
	rms1	rms2	rms3	rms4	rms5	N_{src}	rms1	rms2	rms3	rms4	rms5	N_{src}
(1)	(2)	(3)	(4)	(5)	(6)	(7)	(8)	(9)	(10)	(11)	(12)	(13)
spec1	5.0%	32.5%	20.0%	27.5%	15.0%	40	9.4%	46.9%	28.1%	9.4%	6.2%	32
spec2	17.2%	34.5%	10.3%	24.1%	13.8%	29	19.2%	46.2%	19.2%	3.8%	11.5%	26
spec3	26.4%	37.7%	13.2%	15.1%	7.5%	53	15.7%	43.1%	23.5%	7.8%	9.8%	51
spec4	8.8%	14.7%	17.6%	47.1%	11.8%	34	13.9%	30.6%	30.6%	11.1%	13.9%	36
spec all	15.4%	28.0%	16.1%	28.0%	12.6%	143	15.0%	38.3%	26.3%	9.0%	11.3%	133

NOTE—The definition of each spectral shape are described in Figure 3. The columns are: (1) different time-averaged spectral shape (spec1~spec4); (2)-(7) the proportion of each fractional high-frequency(HF) rms spectral shape (rms1~rms5) in total number of source, several observations of one source showing the same type of the time-averaged spectra and the same type of the rms spectra are classified as one source; (8)-(13) same as column 2-7, but for fractional low-frequency(LF) rms spectra.

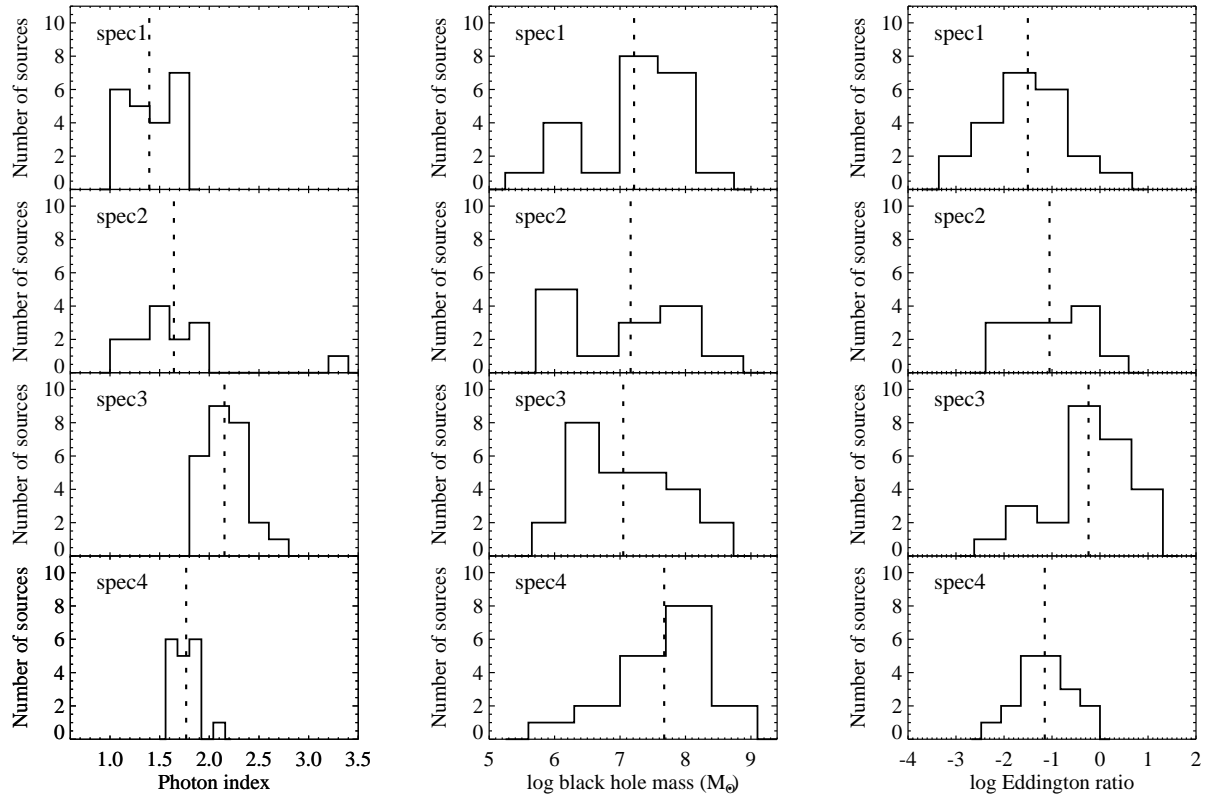


Figure 4. Distribution of the photon index, black hole mass, and Eddington ratio of each source in different time-averaged spectral subgroups. The vertical dashed lines represent the average values.

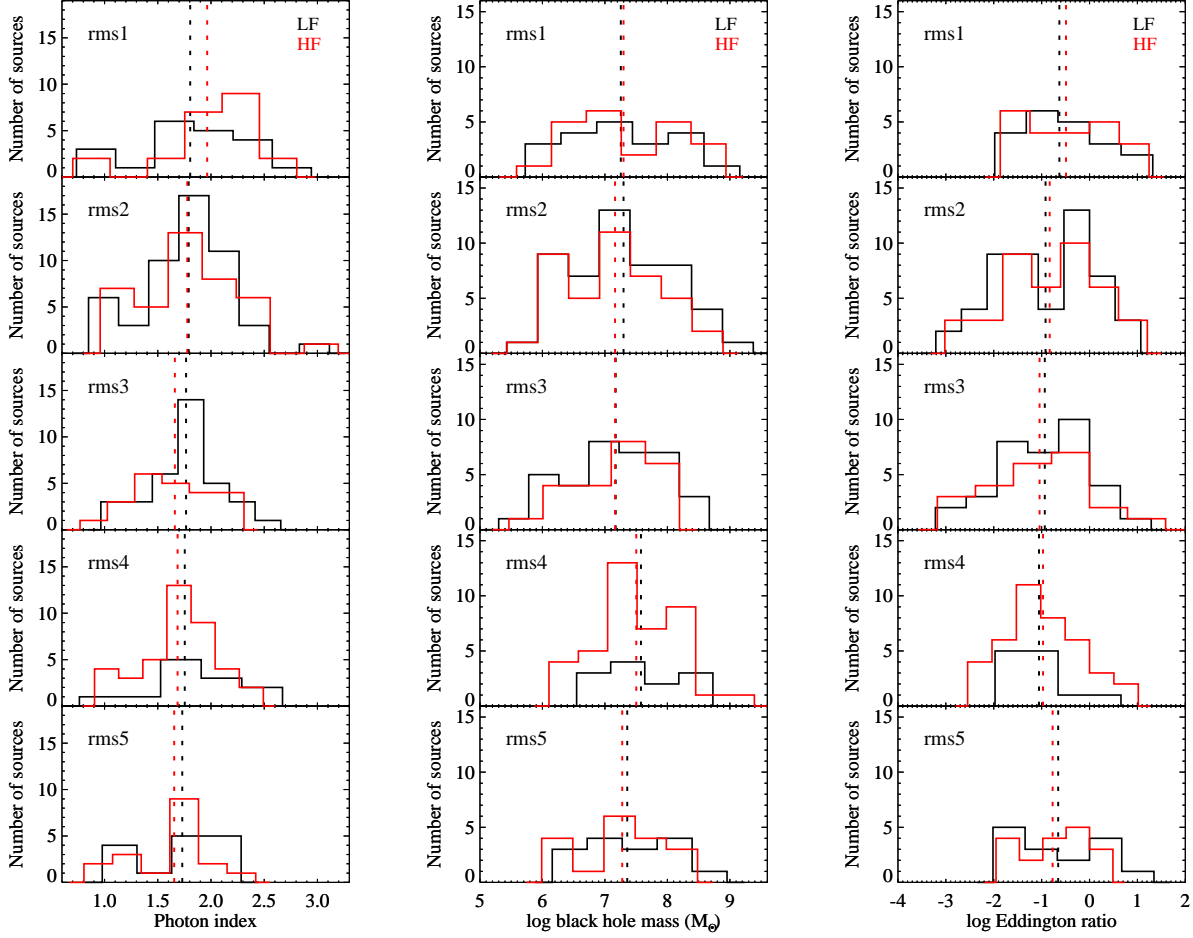


Figure 5. Distribution of the photon index, black hole mass, and Eddington ratio of each source in different rms subgroups. The vertical dashed lines represent the average values. The LF rms subgroups are shown in black lines, and the HF rms subgroups are shown in red lines.

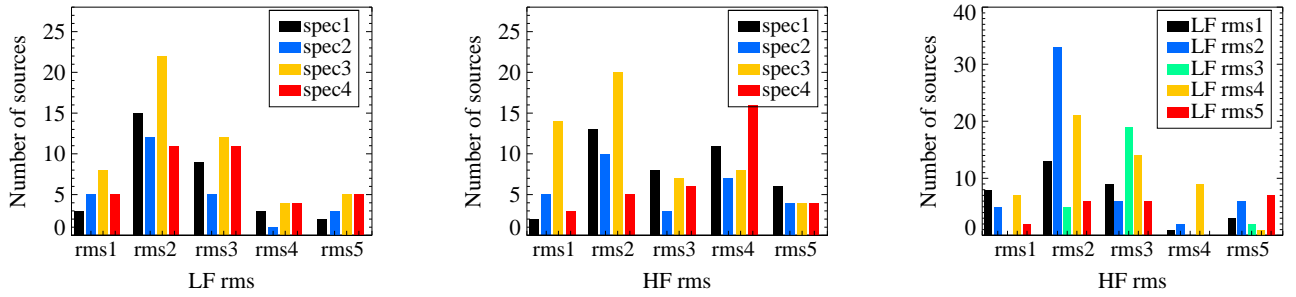


Figure 6. Connection of the rms spectrum and the time-averaged spectrum. Left panel: distribution of the time-averaged spectral classification in different LF rms subsamples. Middle panel: distribution of the time-averaged spectral classification in different HF rms subsamples. Right panel: distribution of the LF rms classification in different HF rms subsamples.

same scenario, the rms2 shape can be understood if in those cases the soft X-ray excess component is not variable, and the hard X-rays contain a less-variable neutral reflection component.

(f) The flattest time-averaged spectra of the spec4 group more difficult to explain. Different combinations of physical processes may be responsible for this spectral shape. We find that in the HF band this spec-

tral group prefers the flat rms spectral shape of rms4, while in the LF band it prefers both rms2 and rms3. Therefore, rms spectra can be used to distinguish different physical models producing similar flat time-averaged spectra.

(g) By comparing the HF and LF rms spectral groups, we find that in most cases the LF and HF rms spectra have similar shapes, which is clearly revealed in Figure 6 right panel. Individual observations can show different combinations of the LF and HF rms spectral shapes. This indicates that the variability properties of individual sources can be very different and complicated.

For some of the systematic connections mentioned above, we have discussed briefly possible physical scenarios which were proposed by previous studies of individual sources. However, this does not mean that these scenarios are exclusive. Indeed, there are different physical scenarios to explain the same combination of spectral shape and variability. For example, both disk-reflection model and wind absorption model are able to explain the spectral-timing properties of 1H 0707-495 (e.g. Kara et al. 2015; Done & Jin 2016; Hagino et al. 2016; Parker et al. 2021). The verification of different X-ray models requires detailed spectral-timing analysis of individual sources, which is beyond the scope of this work.

5. VARIABILITY OF THE FE $K\alpha$ LINE

In many time-averaged spectra, we can visually identify a prominent X-ray Fe $K\alpha$ fluorescence line a rest-frame energy of 6.4 keV (Miller 2007; Netzer 2015). The narrow Fe $K\alpha$ line is often considered to be produced by reprocessing of the central X-ray coronal emission by distant materials such as the dusty torus (Krolik & Kallman 1987; Nandra 2006). The broad Fe $K\alpha$ line is often considered to originate from the innermost part of the accretion disk, with its asymmetric profile caused by the relativistic beaming effect and gravitational redshift (Fabian et al. 1989, 2000). Such a broad component of the Fe $K\alpha$ line has been detected in many AGNs (e.g. Nandra et al. 1997; Miller 2007; Nandra et al. 2007; Patrick et al. 2012; Liu et al. 2015, 2016a; Hu et al. 2019), many of which are also included in our sample. Given the large distance and scale of the reprocessor, it can be inferred that the narrow component may be much less variable than the broad component. Observationally, Bhayani & Nandra (2010) presented an rms variability analysis of a sample of 18 observations of 14 Seyfert galaxies observed by *XMM-Newton*. It is found that the narrow core of the $K\alpha$ line at 6.4 keV shows minimal evidence for variability and is always less variable than the continuum, while

half of observations do show evidence for variations in the wider Fe K band. Thus the LF and HF rms spectra in our sample can be used to distinguish these line components.

5.1. Measuring the Line Flux and Variability

To study the Fe line, the first step is to obtain the best-fitting continuum for each of the objects in the sample. The data below 3 keV are excluded due to the complexity of spectral components in this band. The spectral data in the 5-7 keV range is also masked to avoid any contribution from the Fe K lines. Then we fit the leftover spectra with a power-law model modified by Galactic and any possible intrinsic absorption, which is modeled with the `tbabs*ztbabs*zpowerlaw` model in XSPEC using the cross sections of Verner et al. (1996) and the interstellar medium abundances of Wilms et al. (2000). The underlying continuum can be well fitted with a power law. The excess emission features around 6.4 keV in the AGN rest frame appears to be the Fe K emission lines.

In order to distinguish the line variations from the continuum with sufficient resolution, we rebin the rms spectra and adopt the same set of 11 energy bins ranging from 3 to 10 keV for all the spectra. The same power-law model is applied to these absolute rms spectra, as in the time-averaged spectra. The photon index and normalization are left free to vary. Then the variability around the Fe line region is investigated by deriving the ratio of the rms spectra to the best-fit power-law model. The data-to-model ratios of several typical examples are plotted in Figure 7. The data points marked by the black crosses, red filled dots, and blue filled triangles with error bars represent the time-averaged spectra, and the absolute LF and HF rms spectra, respectively.

5.2. Significance of the Line Flux and Variability

We quantify the significance of the emission line and the line variability by means of Monte Carlo simulations. To examine the reliable detection of the Fe line, i.e. being statistically significant rather than due to random fluctuations, we simulate the ‘observed’ X-ray spectra of the sample sources by assuming no Fe lines, following Liu et al. (2015, see also Liu et al. 2016a,b; Hu et al. 2019). The uncertainty in the best-fitting continuum model itself is also taken into account, following Markowitz et al. (2006, see also Miniutti & Fabian 2006; Tombesi et al. 2010). The basic procedure is: for each of the sources in our sample, we first simulate a spectrum using `fakeit` by assuming the best-fitting continuum model, i.e. the zeroth-order null hypothesis. This fake spectrum is grouped to a minimum of 25

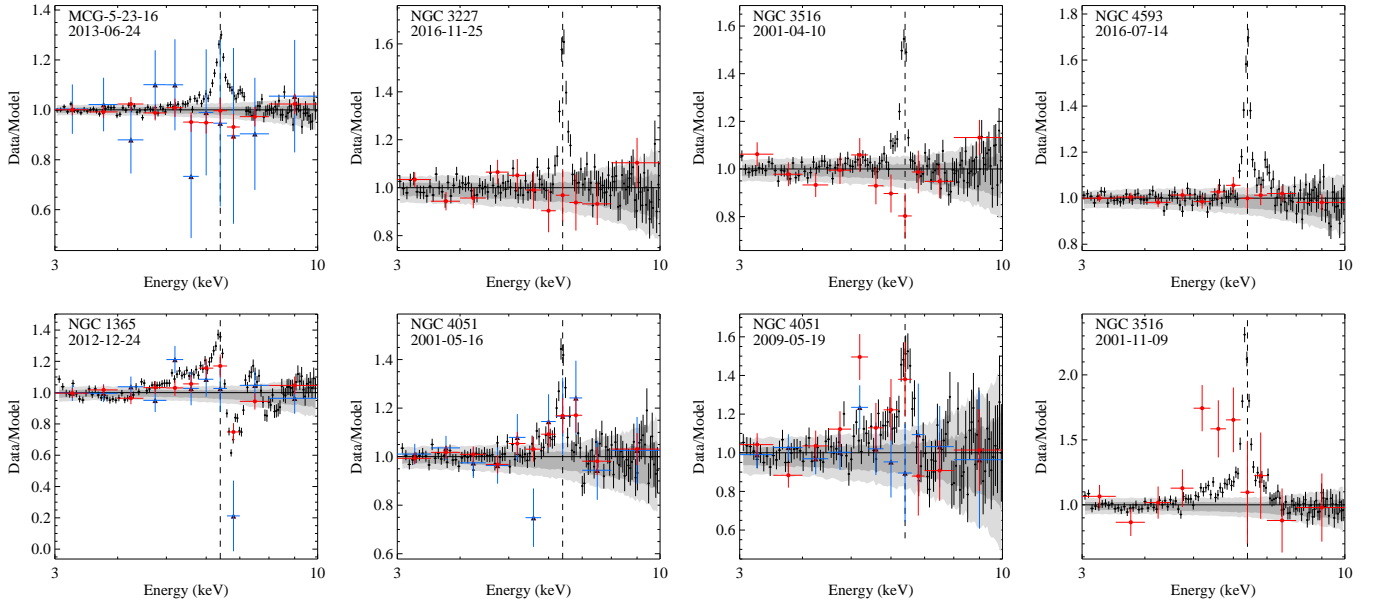


Figure 7. Some examples of the time-averaged spectra (black), LF rms spectra (red), and HF rms spectra (blue) around the Fe $K\alpha$ band. The 1σ and 2σ confidence intervals of the Fe line in the time-averaged spectra are marked as dark and light shaded areas, respectively. The first row shows some examples when a narrow or relatively symmetric Fe line is present, in which case no additional variability is observed. The second row shows some examples when a broad and redshifted Fe line is present in the time-averaged spectra, which is accompanied by additional LF and HF variability.

counts per energy bin for the next step. We fit again this grouped fake spectrum with the null hypothesis model and record the parameter values of the new model, i.e. a refined null hypothesis. Then we simulate a source and a background spectra using `fakeit` by assuming this refined null hypothesis model, which now includes counting statistics uncertainties. For each observation, the same exposure time, auxiliary and redistribution matrix file are used in these simulations to mimic the observed spectrum. The above procedure is repeated 1000 times to produce 1000 simulated spectra for each observation. We can estimate the 1σ (68%) and 2σ (95%) confidence intervals by calculating the 16.0-84.0th and 2.5-97.5th percentile values, respectively in each energy bin, which are shown as the dark and light shadowed areas in Figure 7. It is clear that the emission feature around 6.4 keV is detected significantly in these time-averaged spectra.

To estimate the significance of the Fe line variability, a similar procedure is applied to the rms spectra, which are modeled with a power-law continuum with no emission line components. For every data segment of 100 s bin, the same grouped fake spectrum with the refined null hypothesis model is adopted, which includes the uncertainties of the original best-fitting continuum model. The normalization of the refined null hypothesis model is rescaled so that the total count rate of the model matches the observed count rate in this data segment within 3-5 and 7-10 keV bands. Using this refined null

hypothesis model and taking the random Poisson noise into account, we simulate a new fake spectrum, which provides fluxes in every energy bin. The above tasks are conducted for every data segment, which then allows us to produce fake light curves in every energy bin. Then we perform the same rms variability calculation. Such a procedure is repeated 1000 times, so that the confidence level of rms spectra in each energy bin can be calculated by calculating how many times the simulated rms amplitude is in excess of the observed rms amplitude. An excess in one energy bin is marked as significant if its confidence level exceeds 95%.

5.3. The Diverse Fe Line Variability

An excess emission feature around 6.4 keV (more than three adjacent data bins in excess of the best-fitting continuum) is shown in the majority of the time-averaged spectra of our sample (71 sources with 359 observations, i.e. 91% for source, 84% for observation). When the selection criterion is chosen to be more than three adjacent data bins around 6.4 keV in excess of the 2σ confidence region, the Fe line can be significantly found in $\sim 60\%$ of our sample (48 sources with 241 observations). This is broadly consistent with the result of [Nandra & Pounds \(1994\)](#), who presented an analysis of 60 *Ginga* spectra of 27 Seyfert galaxies and found that Fe lines are detected at $>99\%$ confidence in 37 of the 60 observations, and in 17 of the 27 objects.

Table 4. Number of observations showing variability around the Fe $K\alpha$ line at the 95% confidence level in certain energy bins

Energy bands	LF rms variable	HF rms variable
5.0-6.2 keV	21	9
6.2-6.6 keV	10	2
6.6-7.0 keV	7	1

NOTE—The number of total LF and HF rms spectra in use are 140 and 51, respectively.

Focusing on the Fe line variability, we consider objects with a significant spectral feature around the 6.4 keV region (more than three adjacent data bins in excess of the 2σ confidence region) and fully constrained rms spectra only. This results in 34 sources with a total of 140 *XMM-Newton* observations, including 140 LF rms spectra and 51 HF rms spectra. Then the Fe line variability can be indicated by the significant excess of the rms spectra in this region over the fitted continuum. The statistical results are listed in Table 4.

The narrow Fe $K\alpha$ line is considered to be constant because of the long distance between the reflecting materials (e.g. the torus) and the primary X-ray emission close to the black hole. To check this, we explore the variability in the 6.2-6.6 keV energy band. We find that most observations showing a significant Fe $K\alpha$ line do not show significant LF or HF variability in this energy band (i.e. 49/51 HF rms spectra and 130/140 LF rms spectra show no variability), consistent with previous results (e.g. Bhayani & Nandra 2010). Typical examples are shown in the first row of Figure 7, where the line appears to be narrow, strong, and relatively symmetric, and shows no variability. This is consistent with the physical interpretation of the narrow-line component originating from the reflection of distant materials.

The broad Fe $K\alpha$ line is considered to originate from the inner region of the accretion disk, and its asymmetric profile arises from the relativistic effect close to the black hole. Thus this line component can be more variable than the narrow component. To test this, we explore the excess of the red and blue wings of the Fe $K\alpha$ line in the rms spectra. Indeed, we find that there are about 15%-18% of the sample (9/51 HF rms spectra and 21/140 LF rms spectra) show variability between 5.0-6.2 keV, and about 2%-5% of the sample (1/51 HF rms spectra and 7/140 LF rms spectra) show variability between 6.6-7.0 keV. Typical examples are shown in the second row of Figure 7, where the Fe $K\alpha$ line profile are broad and asymmetric, generally showing an extended

red wing. Despite the relatively low S/N, the rms spectra also exhibit an extended red wing. However, the rms line profile does not follow exactly the time-averaged line profile, indicating further complexities in the line components.

6. DISCUSSION

6.1. Interpretations of Different Rms Spectra

A key result of this work is the discovery of the wide variety of rms spectra in a large sample of Seyferts with a large number of deep observations. The shapes of the rms spectra are found to be frequency-dependent. It should be noted that, as the PSD of AGN is dependent on the black hole mass (e.g. McHardy et al. 2006; Ponti et al. 2012; Pan et al. 2015; González-Martín 2018), the ideal boundary dividing the HF and LF bands may be different from one source to another. The objective of this work is to show the frequency dependence of the rms spectra, and as an approximation we simply chose 10^{-4} Hz as the boundary for all the sources.

Our results reveal that AGN do not only show different time-averaged spectra but also show different rms spectra. Based on previous spectral-timing studies of some individual AGN, we discussed possible interpretations to some specific combinations of the time-averaged spectra and rms spectra, which may help to understand other sources with similar spectral-timing properties.

Firstly, sources in the spec1 group may suffer from severe neutral absorption, but they also show different types of rms spectra. Sources showing both spec1 and rms2 can be explained by the emergence of a stable component in the soft X-ray band, which probably originates from the Compton scattering of distant materials such as the torus (e.g. Arévalo et al. 2014). Another possibility is a stable warm Comptonization component as observed in the soft excess of the NLS1 RE J1034+396 (e.g. Middleton et al. 2011; Jin et al. 2021), but this component may suffer from severely absorption as expected in spec1. In addition, it may also be due to the emergence of large-scale X-ray emission such as photoionized gas (e.g. Härer et al. 2021), scattering, and/or star-formation, as seen in heavily absorbed (e.g. Compton thick) AGN (e.g. LaMassa et al. 2012, 2019). Sources showing spec1, HF rms4, and LF rms3 can be understood if the absorbing materials introduce variability at low frequencies by changing, e.g. the covering factor (Parker et al. 2021).

Secondly, sources in the spec2 group tend to show rms2. This combination of spectral-timing properties is qualitatively consistent with the ionized reflection scenario. In this case, the ionized reflection compo-

ment creates a flux dip at 1-2 keV, which leads to the spec2 shape (e.g. Zoghbi & Fabian 2011; Kara et al. 2013; Jiang et al. 2019). Then as the underlying continuum from the Comptonization of the hot corona contributes more variability, an rms peak emerges at the same energy band which belongs to the rms2 group (Parker et al. 2020). Another scenario is the ionized (warm) absorber (e.g. Crenshaw et al. 2003; Turner et al. 2004), in which case the ionized absorption creates a flux dip at 1-2 keV, and the variation in the ionization state and/or covering fraction introduces additional variability (Parker et al. 2021).

Thirdly, sources in the spec3 group do not show any dip in the flux between 1 and 2 keV, the most common rms for spec3 is rms2, as for spec2. It may due to a variable continuum damped with a less-variable soft excess, more components such as relativistic reflection and/or ultrafast outflow are also included in some cases (e.g. Parker et al. 2021). In addition to the rms2, many sources in the spec3 group show LF rms3 and HF rms1. As mentioned earlier, these properties are typical of some “X-ray simple” super-Eddington NLS1s, such as PG 1244+026 and RX J0439.6-5311, whose X-ray spectra are both steep and smooth, and show a significant soft excess. One physical model to reproduce this type of time-averaged spectrum is the ionized reflection. The smoothness of the spectrum requires the reflection emission to be smeared by the strong relativistic effect, and so an extreme black hole spin is often required (e.g. Zoghbi & Fabian 2011; Kara et al. 2014). However, the simple reflection model is difficult to reproduce the frequency-differentiated rms spectra of these sources (e.g. Jin et al. 2013, 2017a). Another scenario to explain this combination of spectral-timing properties is the warm corona model, where the soft excess is produced by the Comptonization of an extended warm corona, which is distinctive from the compact hard X-ray corona. The different sizes of these two regions lead to different variability timescales, which can explain the stronger LF variability in the soft excess and stronger HF variability in the hard X-rays. It can also explain the LF time lag observed in these sources (e.g. Jin et al. 2013, 2017a, 2021).

As a more quantitative discussion in the framework of the above model, we assume that the X-ray variations may originate from thermal fluctuations in the heating and/or cooling of the gas in the warm and hot corona. The thermal timescale (i.e. the time needed for readjustment to thermal equilibrium) associated with the radiation region can be expressed as,

$$t_{\text{thermal}} \sim \frac{1}{\alpha\Omega} \approx 1.4 \times 10^{-5} \alpha^{-1} M r^{\frac{3}{2}} k_{\Omega}^{-1} \quad (1)$$

(Frank et al. 1992; Kato et al. 2008), in which α is the viscosity parameter, M is the black hole mass in units of M_{\odot} , r is the radius in units of Schwarzschild radius $R_S = 2GM/c^2$ and k_{Ω} is the ratio of angular velocity Ω to the Keplerian velocity Ω_K ($k_{\Omega} = 1$ for the standard Keplerian disk). As a rough estimation, α is set to a typical value of 0.3 and M to the mean value of spec3 subsample of $10^7 M_{\odot}$. For the optically thin hot corona, we employ the solution of the advection-dominated accretion flow (ADAF) of $k_{\Omega} \approx 0.4$ (Yuan & Narayan 2014), then a typical coronal size of a few Schwarzschild radius ($r \sim 3 - 5$) measured from reverberation mapping and gravitational lensing (e.g. Reis & Miller 2013; Fabian et al. 2015; Chartas et al. 2016) leads to $t_{\text{thermal}} \approx 6.1 \times 10^3 - 1.3 \times 10^4$ s, which is broadly consistent with the HF variability timescale ($\sim 10^3 - 10^4$ s). For the warm corona, we take $k_{\Omega} = 1$ for its more disk-like geometry. Also, the warm corona is generally more extended in the radial direction, spanning from $\sim 10R_S$ to several tens of R_S (Jin et al. 2017a). Therefore, for r ranging from 10 to 50, $t_{\text{thermal}} \approx 1.5 \times 10^4 - 1.6 \times 10^5$ s, which may also explain the LF variability ($> 10^4$ s).

We note that the HF variability associated with the hot corona could also be triggered by density fluctuations. The viscous timescale (i.e. the time over which viscosity smooths out surface density gradients) can be expressed as,

$$t_{\text{viscous}} = t_{\text{thermal}} \left(\frac{R}{h}\right)^2 \sim \frac{1}{\alpha\Omega} \left(\frac{R}{h}\right)^2 \quad (2)$$

in which h is the vertical scale-height of the accretion flow. For the geometrically thick ($h \approx R$), ADAF-like hot corona, the viscous timescale is approximately equal to the thermal timescale. The case for the warm corona, however, remains more uncertain due to the poor knowledge of its vertical structure. By comparing the radius of the soft X-ray region and that of the geometrically thick inner disk region dominated by the radiation pressure, Jin et al. (2017a) found tentative evidence for the connection between the warm corona and the puffed-up inner disk, hinting that we may take the scale-height of the inner disk as a reasonable approximation. Specifically, for a radiation pressure dominated Shakura-Sunyaev disk spanning from $\sim 10R_S$ to $50R_S$, the R/h ratio is around $\sim 2 - 6$ at a critical accretion rate $\dot{m} \approx 1$ ($\dot{m} = \dot{M}/\dot{M}_{\text{Edd}}$, $\dot{M}_{\text{Edd}} = 3 \times 10^{-8} m \frac{M_{\odot}}{\text{yr}}$ is the Eddington accretion rate for a Schwarzschild black hole). Consequently, the viscous timescale is expected to be larger than the thermal timescale by a factor of several to several tens, increasing rapidly with the distance to the central black hole. Therefore, we suggest that the density fluctuations in the warm corona may be

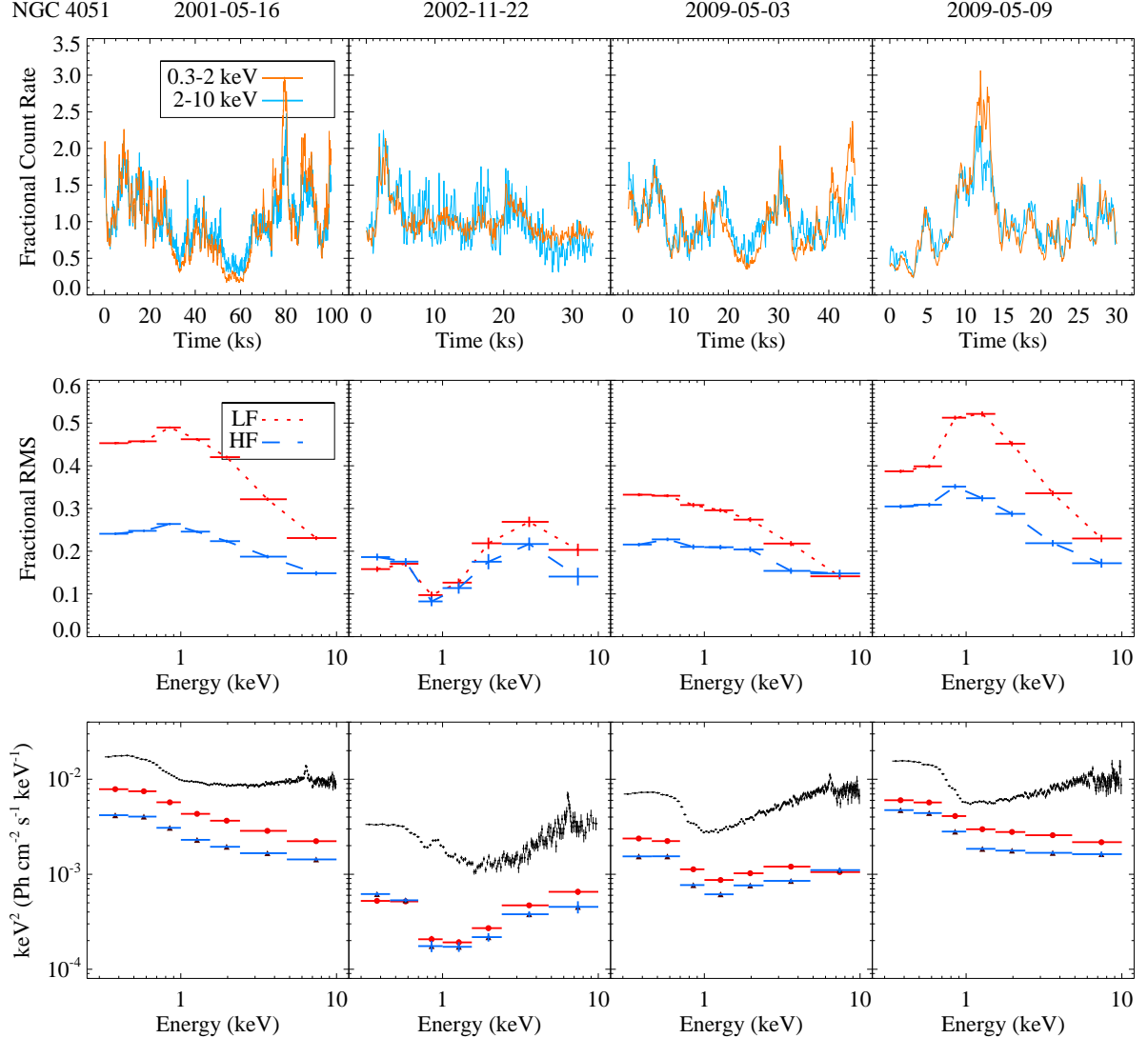


Figure 8. Example of the change in the rms spectral over time for the case of NGC 4051. The top panel shows the fractional count rate variability of 0.3-2 keV and 2-10 keV, shown as orange lines and light blue lines, respectively. The middle panel shows the fractional rms in different frequency ranges. The LF ($< 10^{-4}$ Hz) and the HF ($10^{-4} - 10^{-3}$ Hz) are shown in red dotted lines and blue dashed lines, respectively. The bottom panel shows the time-averaged spectrum (black crosses) and absolute rms spectra in the case of LF (red filled dots) and HF (blue filled triangle).

responsible for the variability at a longer timescale than those concerned in this work, except for those emerging at innermost regions, or in some super-accreting systems with very high accretion rates (the scale-height depends linearly on the accretion rate for a radiation pressure dominated disk, $h \propto \dot{m}$, Shakura & Sunyaev 1973). It should be noted that the above calculations are only order-of-magnitude estimates and the obtained values are subject to large uncertainties.

The above interpretations are simply based on previous studies of a few individual sources. As different combinations of time-averaged spectra and rms spectra may correspond to different physical mechanisms,

further studies are required in order to interpret other combinations.

6.2. Variation of the Rms in Individual Sources

Recent studies on individual sources have shown that the rms spectrum and power spectrum can change significantly as the time-averaged spectrum changes between observations (e.g. Parker et al. 2021; Yang et al. 2022). As shown in Table 1, the majority of our sample have multiple observations, which allows us to investigate the variability of the rms spectra in these sources.

Figure 8 shows NGC 4051 as a typical example. Its rms spectra change significantly as the time-averaged

spectra change. During the first *XMM-Newton* observation in 2001 May 16, both fractional LF and HF rms spectra display a concave-down shape peaking at 1-2 keV. Then during the observation in 2002 November 22, the flux of the time-averaged spectra decreases by almost 1 order of magnitude, and the fractional rms in both LF and HF bands are strongly suppressed below 3 keV. During the third observation in 2009 May 03, the flux recovers by a factor of few, and the rms in LF and HF are also observed to increase. During the fourth observation in 2009 May 09, the time-averaged spectrum and the LF and HF rms spectra all return to a similar state as the first observation. This example clearly reveals the connection of the variation between the rms and time-averaged spectra in individual sources. A possible physical interpretation is that the photoionized gas emission on large scale dominates the soft X-ray band at low fluxes, as at high fluxes the continuum dominates and the contribution from photoionized gas is negligible, similar to the recent study on 1H 0707-495 by Parker et al. (2021). In addition, it may also be due to the variability of the ionized absorption along the line of sight. However, the Eddington ratio of NGC 4051 is quite low, so the absorber may have different properties. Based on the study of our sample, we point out that the covariation in the rms and time-averaged spectra is common, as shown in Figure A2 in the appendix, but a more detailed study of individual sources is beyond the scope of this work.

6.3. Origin of the Fe $K\alpha$ Line

About 60% of the time-averaged spectra of our sample exhibit a significant spectral feature around 6.4 keV, for which the rms spectra with small energy bins around this region are produced. The majority of the Fe line shows no significant variability in the HF and LF rms spectra, partly due to the relatively low count rate in this energy band. Interestingly, we do detect significant variability in 140 observations of 34 sources.

The narrow Fe $K\alpha$ line is commonly present in AGN spectra and is thought to be the fluorescence emission from distant materials such as the dusty torus. It is not expected to show strong variability, which is consistent with our results. The broad Fe $K\alpha$ line is believed to be produced by the reflection of corona emission in the inner disk region (e.g. Kara et al. 2013; Fabian et al. 2013; Kara et al. 2015). In this scenario, the reflection should respond rapidly to the change in the corona, so that significant variability is expected in the broad Fe $K\alpha$ line. Indeed, significant time lags have been reported for a sample of Seyferts (De Marco et al. 2013; Kara et al. 2016).

Despite the relatively low S/N, we notice that the rms spectra of the Fe $K\alpha$ line do not show similar profiles as the time-averaged spectra; this suggests that the Fe $K\alpha$ line profile may contain various components of different variability properties, similar to the properties of hydrogen Balmer lines in the optical (e.g. Peterson et al. 2004). Next generation telescopes such as *Athena* (Nandra et al. 2013) and *eXTP* (Zhang et al. 2016) will be able to provide data with much higher S/N to reveal more detailed properties of the Fe $K\alpha$ line.

7. SUMMARY AND CONCLUSION

We have conducted a systematic study of the X-ray variability for a large sample of 78 Seyfert galaxies observed with 426 deep *XMM-Newton* observations. In this paper, we focus on the rms spectra in both low and high-frequency bands. The main results are summarized below.

1. We find that the calculation of the intrinsic rms is sensitive to the subtraction of the Poisson noise power. The adoption of theoretical Poisson noise power can lead to significant underestimate of the true Poisson noise due to various corrections applied to the observed light curve. Thus the intrinsic rms can be overestimated. Although it is possible to apply further corrections, we suggest that the most accurate method is to calculate the arithmetic average of the power in the HF band where the Poisson noise power dominates.
2. We find a wide variety of rms spectra and time-averaged spectra in the sample. Our statistical study of the sample confirms the correlation between the Eddington ratio and the steepness of the time-averaged spectra. We also find that sources with the largest black hole masses and low Eddington ratios in our sample tend to show both flat rms spectra and time-averaged spectra.
3. There exist various combinations of the time-averaged spectra and rms spectra, i.e. there is no one-to-one mapping between different subtypes of the time-averaged spectra and rms spectra. The same time-averaged spectra can have different rms spectra, while the same rms spectra can be accompanied by different time-averaged spectra.
4. The most common rms spectral shape is the one which has a concave-down shape with an rms peak at ~ 1 keV (rms2). The rarest rms shape is the one which has a concave-up shape with an rms minimal at ~ 1 keV (rms5). The shape of rms2 is qualitatively consistent with the rms pattern introduced by the ionized

reflection or the ionized absorption, while the shape of rms5 is qualitatively consistent with the rms pattern introduced by the photoionized gas emission on large scale.

5. Comparing the time-averaged spectral groups of spec1, 2, and 3, we find that they all prefer the rms2 spectral shape, but there are also systematic differences among the three spectral groups in terms of both observed properties and theoretical interpretations. For spec1, the HF rms spectra tend to be flat, and the LF rms spectra tend to show more fractional rms towards soft X-rays. This indicates that neutral absorption cannot introduce additional HF variability but may introduce LF variability. For spec2, the spectral-timing properties can be interpreted as a variable power law damped with a less-variable soft excess which may (or may not) be associated with relativistic reflection and/or a warm corona. For spec3 with the highest Eddington ratio, the soft X-rays tend to show weaker HF rms, while the hard X-rays tend to show stronger HF rms. These properties are similar to those found in super-Eddington NLS1s and are consistent with the warm Comptonization model for the soft excess.
6. Significant variability is detected at the Fe $K\alpha$ line energies in 34 Seyferts with 140 observations. We find that broad Fe $K\alpha$ lines with a redshifted-wing tend to show significant variability, which is likely because the line originates from disk reflection close to the black

hole. The narrow Fe $K\alpha$ line with a symmetric line profile is much less variable, which is consistent with the distant reflection model.

Our results show that the detailed variability analysis can provide an important diagnostics, complementary to the time-averaged spectral analysis. Thus a joint spectral-timing analysis is valuable for the understanding of the X-ray radiation mechanisms of AGN. To make such a study easier for the community and to make the most of the valuable *XMM-Newton* observational data, we have made all the time-averaged spectra and HF/LF rms spectra of the entire sample publicly available on our website⁴.

ACKNOWLEDGMENTS

We thank the anonymous referee providing valuable comments and suggestions, which have improved the quality of the paper. C.J. acknowledges Wenda Zhang for valuable discussions. This work is supported by the National Natural Science Foundation of China (grant Nos.11773037, 11673026, 11473035, 11873054, 11803047, 12173048), the gravitational wave pilot B (grant No.XDB23040100), the Strategic Pioneer Program on Space Science, Chinese Academy of Sciences, grant No.XDA15052100. This work is based on observations conducted by *XMM-Newton*, an ESA science mission with instruments and contributions directly funded by ESA Member States and the USA (NASA).

REFERENCES

- Ai, Y. L., Yuan, W., Zhou, H. Y., Wang, T. G., & Zhang, S. H. 2011, *ApJ*, 727, 31
- Alston, W. N., Fabian, A. C., Kara, E., et al. 2020, *Nature Astronomy*, 4, 597
- Arévalo, P., McHardy, I. M., Markowitz, A., et al. 2008, *MNRAS*, 387, 279
- Arévalo, P., Bauer, F. E., Puccetti, S., et al. 2014, *ApJ*, 791, 81
- Belloni, T., & Hasinger, G. 1990, *A&A*, 227, L33
- Bentz, M. C., Cackett, E. M., Crenshaw, D. M., et al. 2016, *ApJ*, 830, 136
- Bentz, M. C., Walsh, J. L., Barth, A. J., et al. 2009, *ApJ*, 705, 199
- Bentz, M. C., Horenstein, D., Bazhaw, C., et al. 2014, *ApJ*, 796, 8
- Bhayani, S., & Nandra, K. 2010, *MNRAS*, 408, 1020
- Bian, W., & Zhao, Y. 2003, *MNRAS*, 343, 164
- Busch, G., Zuther, J., Valencia-S., M., et al. 2014, *A&A*, 561, A140
- Cackett, E. M., Fabian, A. C., Zoghbi, A., et al. 2013, *ApJL*, 764, L9
- Chartas, G., Rhea, C., Kochanek, C., et al. 2016, *Astronomische Nachrichten*, 337, 356
- Cheng, H., Yuan, W., Liu, H.-Y., et al. 2019, *MNRAS*, 487, 3884
- Crenshaw, D. M., Kraemer, S. B., & George, I. M. 2003, *ARA&A*, 41, 117
- Crummy, J., Fabian, A. C., Gallo, L., & Ross, R. R. 2006, *MNRAS*, 365, 1067
- Czerny, B., Rózańska, A., & Kuraszkiewicz, J. 2004, *A&A*, 428, 39
- De Marco, B., Ponti, G., Cappi, M., et al. 2013, *MNRAS*, 431, 2441

⁴ <https://gohujingwei.github.io/rms.html>. All the spectral files can be downloaded directly for joint modeling in XSPEC.

- De Marco, B., Adhikari, T. P., Ponti, G., et al. 2020, *A&A*, 634, A65
- Denney, K. D., Bentz, M. C., Peterson, B. M., et al. 2006, *ApJ*, 653, 152
- Done, C., Davis, S. W., Jin, C., Blaes, O., & Ward, M. 2012, *MNRAS*, 420, 1848
- Done, C., & Jin, C. 2016, *MNRAS*, 460, 1716
- Du, P., Hu, C., Lu, K.-X., et al. 2014, *ApJ*, 782, 45
- Edelson, R., Turner, T. J., Pounds, K., et al. 2002, *ApJ*, 568, 610
- Fabbiano, G. 1989, *ARA&A*, 27, 87
- Fabian, A. C., Iwasawa, K., Reynolds, C. S., & Young, A. J. 2000, *PASP*, 112, 1145
- Fabian, A. C., Lohfink, A., Kara, E., et al. 2015, *MNRAS*, 451, 4375
- Fabian, A. C., Rees, M. J., Stella, L., & White, N. E. 1989, *MNRAS*, 238, 729
- Fabian, A. C., Vaughan, S., Nandra, K., et al. 2002, *MNRAS*, 335, L1
- Fabian, A. C., Kara, E., Walton, D. J., et al. 2013, *MNRAS*, 429, 2917
- Frank, J., King, A., & Raine, D. 1992, *Accretion power in astrophysics.*, Vol. 21
- Gallo, L. C. 2006, *MNRAS*, 368, 479
- Gardner, E., & Done, C. 2014, *MNRAS*, 442, 2456
- Gaskell, C. M. 2004, *ApJL*, 612, L21
- Giozzi, M., Papadakis, I. E., Grupe, D., et al. 2010, *ApJ*, 717, 1243
- González-Martín, O. 2018, *ApJ*, 858, 2
- Grupe, D., Komossa, S., Leighly, K. M., & Page, K. L. 2010, *ApJS*, 187, 64
- Haardt, F., & Maraschi, L. 1991, *ApJL*, 380, L51
- Hagino, K., Odaka, H., Done, C., et al. 2016, *MNRAS*, 461, 3954
- Härer, L., Parker, M. L., Joyce, A., et al. 2021, *MNRAS*, 500, 4506
- HI4PI Collaboration, Ben Bekhti, N., Flöer, L., et al. 2016, *A&A*, 594, A116
- Hu, J., Liu, Z., Jin, C., & Yuan, W. 2019, *MNRAS*, 488, 4378
- Husemann, B., Scharwächter, J., Davis, T. A., et al. 2019, *A&A*, 627, A53
- Iwasawa, K., Fabian, A. C., Kara, E., et al. 2016, *A&A*, 592, A98
- Jansen, F., Lumb, D., Altieri, B., et al. 2001, *A&A*, 365, L1
- Jiang, J., Fabian, A. C., Dauser, T., et al. 2019, *MNRAS*, 489, 3436
- Jin, C., Done, C., Middleton, M., & Ward, M. 2013, *MNRAS*, 436, 3173
- Jin, C., Done, C., & Ward, M. 2016, *MNRAS*, 455, 691
- . 2017a, *MNRAS*, 468, 3663
- . 2020, *MNRAS*, 495, 3538
- . 2021, *MNRAS*, 500, 2475
- Jin, C., Done, C., Ward, M., & Gardner, E. 2017b, *MNRAS*, 471, 706
- Jin, C., Done, C., Ward, M., Gierliński, M., & Mullaney, J. 2009, *MNRAS*, 398, L16
- Jin, C., Ward, M., Done, C., & Gelbord, J. 2012, *MNRAS*, 420, 1825
- Kara, E., Alston, W. N., Fabian, A. C., et al. 2016, *MNRAS*, 462, 511
- Kara, E., Cackett, E. M., Fabian, A. C., Reynolds, C., & Uttley, P. 2014, *MNRAS*, 439, L26
- Kara, E., Fabian, A. C., Cackett, E. M., et al. 2013, *MNRAS*, 428, 2795
- Kara, E., Fabian, A. C., Lohfink, A. M., et al. 2015, *MNRAS*, 449, 234
- Kato, S., Fukue, J., & Mineshige, S. 2008, *Black-Hole Accretion Disks — Towards a New Paradigm —*
- Kosec, P., Buisson, D. J. K., Parker, M. L., et al. 2018, *MNRAS*, 481, 947
- Krolik, J. H., & Kallman, T. R. 1987, *ApJL*, 320, L5
- Laha, S., Ghosh, R., Guainazzi, M., & Markowitz, A. G. 2018, *MNRAS*, 480, 1522
- LaMassa, S. M., Heckman, T. M., & Ptak, A. 2012, *ApJ*, 758, 82
- LaMassa, S. M., Yaqoob, T., Boorman, P. G., et al. 2019, *ApJ*, 887, 173
- Laor, A. 1998, *ApJL*, 505, L83
- Laor, A., Fiore, F., Elvis, M., Wilkes, B. J., & McDowell, J. C. 1997, *ApJ*, 477, 93
- León Tavares, J., Kotilainen, J., Chavushyan, V., et al. 2014, *ApJ*, 795, 58
- Lewis, K. T., & Eracleous, M. 2006, *ApJ*, 642, 711
- Liu, H., Parker, M. L., Jiang, J., et al. 2021, *MNRAS*, 506, 5190
- Liu, H.-Y., Liu, W.-J., Dong, X.-B., et al. 2019, *ApJS*, 243, 21
- Liu, Z., Yuan, W., Lu, Y., et al. 2016a, *MNRAS*, 463, 684
- Liu, Z., Yuan, W., Lu, Y., & Zhou, X. 2015, *MNRAS*, 447, 517
- Liu, Z., Merloni, A., Georgakakis, A., et al. 2016b, *MNRAS*, 459, 1602
- Longinotti, A. L., Vega, O., Krongold, Y., et al. 2018, *ApJL*, 867, L11
- Lu, Y., & Yu, Q. 1999, *ApJL*, 526, L5
- Magdziarz, P., Blaes, O. M., Zdziarski, A. A., Johnson, W. N., & Smith, D. A. 1998, *MNRAS*, 301, 179
- Malizia, A., Bassani, L., Bird, A. J., et al. 2008, *MNRAS*, 389, 1360

- Markowitz, A., Edelson, R., & Vaughan, S. 2003, *ApJ*, 598, 935
- Markowitz, A., Papadakis, I., Arévalo, P., et al. 2007, *ApJ*, 656, 116
- Markowitz, A., Reeves, J. N., & Braito, V. 2006, *ApJ*, 646, 783
- McHardy, I. M., Koering, E., Knigge, C., Uttley, P., & Fender, R. P. 2006, *Nature*, 444, 730
- Middleton, M., Done, C., Ward, M., Gierliński, M., & Schurch, N. 2009, *MNRAS*, 394, 250
- Middleton, M., Uttley, P., & Done, C. 2011, *MNRAS*, 417, 250
- Miller, J. M. 2007, *ARA&A*, 45, 441
- Miniutti, G., & Fabian, A. C. 2004, *MNRAS*, 349, 1435
- . 2006, *MNRAS*, 366, 115
- Nandra, K. 2006, *MNRAS*, 368, L62
- Nandra, K., George, I. M., Mushotzky, R. F., Turner, T. J., & Yaqoob, T. 1997, *ApJ*, 477, 602
- Nandra, K., O’Neill, P. M., George, I. M., & Reeves, J. N. 2007, *MNRAS*, 382, 194
- Nandra, K., & Pounds, K. A. 1994, *MNRAS*, 268, 405
- Nandra, K., Barret, D., Barcons, X., et al. 2013, *arXiv e-prints*, arXiv:1306.2307
- Netzer, H. 2015, *ARA&A*, 53, 365
- Pan, H.-W., Yuan, W., Zhou, X.-L., Dong, X.-B., & Liu, B. 2015, *ApJ*, 808, 163
- Pancoast, A., Brewer, B. J., Treu, T., et al. 2014, *MNRAS*, 445, 3073
- Parker, M. L., Alston, W. N., Igo, Z., & Fabian, A. C. 2020, *MNRAS*, 492, 1363
- Parker, M. L., Marinucci, A., Brenneman, L., et al. 2014, *MNRAS*, 437, 721
- Parker, M. L., Fabian, A. C., Matt, G., et al. 2015, *MNRAS*, 447, 72
- Parker, M. L., Alston, W. N., Härer, L., et al. 2021, *MNRAS*, 508, 1798
- Patrick, A. R., Reeves, J. N., Porquet, D., et al. 2012, *MNRAS*, 426, 2522
- Peterson, B. M., Ferrarese, L., Gilbert, K. M., et al. 2004, *ApJ*, 613, 682
- Peterson, B. M., Bentz, M. C., Desroches, L.-B., et al. 2005, *ApJ*, 632, 799
- Ponti, G., Papadakis, I., Bianchi, S., et al. 2012, *A&A*, 542, A83
- Poutanen, J., Zdziarski, A. A., & Ibragimov, A. 2008, *MNRAS*, 389, 1427
- Press, W. H., Teukolsky, S. A., Vetterling, W. T., & Flannery, B. P. 1992, *Numerical recipes in FORTRAN. The art of scientific computing*
- Qiao, E., & Liu, B. F. 2018, *MNRAS*, 477, 210
- Ranalli, P., Comastri, A., & Setti, G. 2003, *A&A*, 399, 39
- Reis, R. C., & Miller, J. M. 2013, *ApJL*, 769, L7
- Revnivtsev, M., Gilfanov, M., & Churazov, E. 1999, *A&A*, 347, L23
- Revnivtsev, M., Fabrika, S., Abolmasov, P., et al. 2006, *A&A*, 447, 545
- Risaliti, G., Miniutti, G., Elvis, M., et al. 2009, *ApJ*, 696, 160
- Ross, R. R., & Fabian, A. C. 2005, *MNRAS*, 358, 211
- Shakura, N. I., & Sunyaev, R. A. 1973, *A&A*, 500, 33
- Shemmer, O., Brandt, W. N., Netzer, H., Maiolino, R., & Kaspi, S. 2008, *ApJ*, 682, 81
- Sobolewska, M. A., & Życki, P. T. 2006, *MNRAS*, 370, 405
- Tatum, M. M., Turner, T. J., Sim, S. A., et al. 2012, *ApJ*, 752, 94
- Taylor, R. D., Uttley, P., & McHardy, I. M. 2003, *MNRAS*, 342, L31
- Timmer, J., & Koenig, M. 1995, *A&A*, 300, 707
- Tombesi, F., Cappi, M., Reeves, J. N., et al. 2010, *A&A*, 521, A57
- Tran, H. D., Lyke, J. E., & Mader, J. A. 2011, *ApJL*, 726, L21
- Trump, J. R., Impey, C. D., Kelly, B. C., et al. 2011, *ApJ*, 733, 60
- Turner, A. K., Fabian, A. C., Lee, J. C., & Vaughan, S. 2004, *MNRAS*, 353, 319
- Turner, T. J., Miller, L., Reeves, J. N., & Kraemer, S. B. 2007, *A&A*, 475, 121
- Uttley, P., Cackett, E. M., Fabian, A. C., Kara, E., & Wilkins, D. R. 2014, *A&A Rv*, 22, 72
- Uttley, P., & McHardy, I. M. 2001, *MNRAS*, 323, L26
- Uttley, P., McHardy, I. M., & Vaughan, S. 2005, *MNRAS*, 359, 345
- Vasudevan, R. V., & Fabian, A. C. 2009, *MNRAS*, 392, 1124
- Vasudevan, R. V., Fabian, A. C., Gandhi, P., Winter, L. M., & Mushotzky, R. F. 2010, *MNRAS*, 402, 1081
- Vasudevan, R. V., Mushotzky, R. F., Winter, L. M., & Fabian, A. C. 2009, *MNRAS*, 399, 1553
- Vasylenko, A. A. 2018, *Ap&SS*, 363, 228
- Vaughan, S., Edelson, R., Warwick, R. S., & Uttley, P. 2003, *MNRAS*, 345, 1271
- Vaughan, S., & Fabian, A. C. 2004, *MNRAS*, 348, 1415
- Verner, D. A., Ferland, G. J., Korista, K. T., & Yakovlev, D. G. 1996, *ApJ*, 465, 487
- Wang, J., Mao, Y. F., & Wei, J. Y. 2009, *AJ*, 137, 3388
- Wang, J.-M., Watarai, K.-Y., & Mineshige, S. 2004, *ApJL*, 607, L107
- Wang, J.-M., & Zhang, E.-P. 2007, *ApJ*, 660, 1072
- Wang, J.-M., Du, P., Hu, C., et al. 2014, *ApJ*, 793, 108

- Wang, T., & Lu, Y. 2001, *A&A*, 377, 52
- Williams, J. K., Gliozzi, M., & Rudzinsky, R. V. 2018, *MNRAS*, 480, 96
- Wilms, J., Allen, A., & McCray, R. 2000, *ApJ*, 542, 914
- Woo, J.-H., & Urry, C. M. 2002, *ApJ*, 579, 530
- Yang, H., Jin, C., & Yuan, W. 2022, arXiv e-prints, arXiv:2207.12151
- Yuan, F., & Narayan, R. 2014, *ARA&A*, 52, 529
- Zhang, E.-P., & Wang, J.-M. 2006, *ApJ*, 653, 137
- Zhang, S. N., Feroci, M., Santangelo, A., et al. 2016, in *Society of Photo-Optical Instrumentation Engineers (SPIE) Conference Series*, Vol. 9905, *Space Telescopes and Instrumentation 2016: Ultraviolet to Gamma Ray*, ed. J.-W. A. den Herder, T. Takahashi, & M. Bautz, 99051Q
- Zhou, X.-L., & Wang, J.-M. 2005, *ApJL*, 618, L83
- Zoghbi, A., & Fabian, A. C. 2011, *MNRAS*, 418, 2642

APPENDIX

A. THE FREQUENCY-RESOLVED RMS SPECTRA

A.1. Calculation of the Rms Spectra

The fractional rms amplitude (Edelson et al. 2002; Markowitz et al. 2003; Vaughan et al. 2003) is a common measure of the intensity of intrinsic source variability. In this work, we adopt the frequency-resolved spectral techniques developed by Revnivtsev et al. (1999) to calculate the rms from X-ray light curves. We summarize the calculation procedure below (see also Vaughan et al. 2003; Poutanen et al. 2008; Jin et al. 2017a). A detailed prescription can also be found in Arévalo et al. (2008).

The PSD quantifies the amount of variability power as a function of frequency. A periodogram, which is a single realization of a PSD, can be obtained through the discrete Fourier transform (DFT; Press et al. 1992) of a light curve as,

$$P(f_i) = \frac{2\Delta T}{N\bar{x}^2} |\text{DFT}(f_i)|^2 = \frac{2\Delta T}{N\bar{x}^2} \left| \sum_{j=1}^N x_j e^{2\pi i f_i t_j} \right|^2 \quad (\text{A1})$$

where the power density $P(f_i)$ is in units of Hz^{-1} , ΔT is the time bin of the light curve, N is the number of useful time bins, \bar{x} is the average count rate of the light curve $x(t_j)$, f_i is the Fourier frequency defined as $f_i = i/T$. Each light curve is binned in 100 s and thus gives a Nyquist frequency (i.e. the upper limit of the frequency range of a periodogram) of 5×10^{-3} Hz. Moreover, we divide the frequency range into two subranges, and define 10^{-4} Hz $< f \leq 10^{-3}$ Hz as the HF band and $f \leq 10^{-4}$ Hz as the LF band.

As we adopt the Belloni-Hasinger normalization (Belloni & Hasinger 1990) in Equation A1, the normalized excess variance σ_{NXS}^2 can be calculated by integrating the periodogram over a specific frequency range after subtracting the Poisson noise power (Arévalo et al. 2008),

$$\sigma_{\text{NXS},\Delta f}^2 = \sum_{i=a}^b (P(f_i) - \text{PN}_{\text{lev}}) \delta f \quad (\text{A2})$$

where Δf is the frequency range of $\Delta f = b/T - a/T$, δf is defined as $\delta f = 1/T$, PN_{lev} is the Poisson noise contribution calculated by averaging the power density in the frequency range of larger than 2×10^{-3} Hz, where the Poisson noise power dominates. Full details of the Poisson noise calculation are given in Section A.2. Then the fractional rms $\sigma_{\text{rms},\Delta f}$ can be calculated as,

$$\sigma_{\text{rms},\Delta f} = \sqrt{\sum_{i=a}^b (P(f_i) - \text{PN}_{\text{lev}}) \delta f} \quad (\text{A3})$$

The error of σ_{rms} can be calculated using the following equation (Poutanen et al. 2008),

$$\text{err}(\sigma_{\text{rms},\Delta f}) = \sqrt{\sigma_{\text{NXS},\Delta f}^2 + \text{err}(\sigma_{\text{NXS},\Delta f}^2)} - \sigma_{\text{rms},\Delta f} \quad (\text{A4})$$

where $\text{err}(\sigma_{\text{NXS},\Delta f}^2)$ can be calculated as,

$$\text{err}(\sigma_{\text{NXS},\Delta f}^2) = \sqrt{\left(\frac{\text{PN}_{\text{lev}} \times \Delta f}{\sqrt{N'}}\right)^2 + \frac{2\text{PN}_{\text{lev}} \times \Delta f \sigma_{\text{NXS},\Delta f}^2}{N'}} \quad (\text{A5})$$

where N' is the number of frequency points within Δf in the periodogram.

Then the absolute rms spectra can be calculated by multiplying the fractional rms by the average count rate in each energy bin. The resultant absolute rms spectra can be fitted in XSPEC using the same response and ancillary files of the time-averaged spectra (e.g. Revnivtsev et al. 2006; Sobolewska & Życki 2006; Middleton et al. 2011; Jin et al. 2013). The variable component of a time-averaged spectrum in the LF and HF bands can be revealed directly by the

corresponding absolute rms spectra. This means that if a time-averaged spectrum comprises several components with different variability properties in different frequency bands, then a joint modeling of the time-averaged spectra and absolute rms spectra can help to distinguish these components (e.g. Jin et al. 2013, 2016, 2017a; Parker et al. 2020; Jin et al. 2020; Parker et al. 2021).

A.2. Determination of the Poisson Noise Power

A PSD comprises the power of both the intrinsic source variability and the Poisson noise, and so the subtraction of Poisson noise power can affect the accuracy of the intrinsic rms of the source. This is especially important when the signal-to-noise of the light curve is low, either due to the low source flux or the narrow energy band. To this end, we investigate the accuracy of various methods for the estimation of Poisson noise power, and test their impact on the resultant rms.

The Poisson noise power is supposed to be a constant component in the PSD at a theoretical level of $\text{PN}_{\text{lev}} = 2/\bar{x}$, where \bar{x} is the average source count rate. If we also consider the background subtraction, then PN_{lev} can be calculated as (Arévalo et al. 2008),

$$\text{PN}_{\text{lev}} = \frac{2(\bar{x} + \bar{b})}{\bar{x}^2} \quad (\text{A6})$$

where \bar{b} is the average count rate of the background underneath the source extraction region. It must be noted that the background light curve also contains Poisson noise power; thus during the background subtraction, the noise of background will also propagate into the final light curve. This means that in reality Equation A6 underestimates the Poisson noise power, unless the background can be perfectly determined.

However, our source light curves are produced by the `epiclccorr` task in the `SAS` software, which performs absolute corrections, relative corrections that are time-dependent, and background subtraction⁵. For example, our source extraction region only covers a fraction of the PSF; thus a correction factor larger than unity will be applied to the source light curve in order to recover the intrinsic source flux. Therefore, the theoretical PN_{lev} calculated from Equation A6 for a corrected light curve will be smaller than the true PN_{lev} contained in the light curve, and then the resultant fractional rms will be biased to a larger value. We demonstrate this effect in Figure A1, which shows the periodograms of two sources. The cyan solid line indicates the Poisson noise power calculated from Equation A6, which is clearly smaller than the constant white-noise power observed at high frequencies. We also note that this effect was never mentioned in previous literatures, and so we urge caution to be exercised in dealing with this effect.

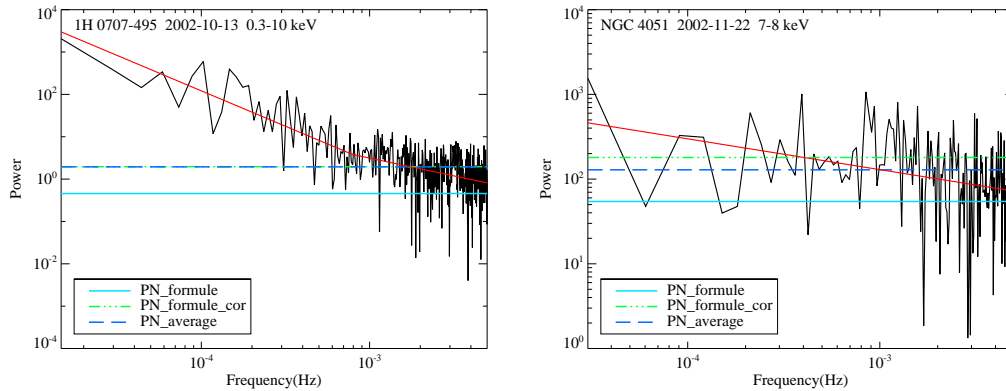


Figure A1. Two examples of the PSD results. The best-fitted broken power laws are shown in red solid lines. The other horizontal lines mark the Poisson noise calculated from various method. The cyan solid lines represent the common formula, $\text{PN}_{\text{lev}} = 2(\bar{x} + \bar{b})/\bar{x}^2$, where \bar{b} is the average count rate of the background, and \bar{x} is the average count rate of the background-subtracted light curve. The green dotted-dotted-dotted-dashed lines represent the correction of this formula, $\text{PN}_{\text{lev_cor}} = 2((\bar{x}/\bar{f}) + \bar{b})/(\bar{x}/\bar{f})^2$, where \bar{f} is the mean PSF correction factor. The blue dashed lines represent the arithmetic average of the power over the PSD frequency range of above 2×10^{-3} Hz.

⁵ <https://heasarc.gsfc.nasa.gov/docs/xmm/sas/help/epiclccorr/index.html>

In order to recover the true PN_{lev} , we can replace \bar{x} with \bar{x}/f in Equation A6, where f is the correction factor applied to the background-subtracted source light curve. However, it is difficult to know an accurate f because it is calculated by `epiclccorr` internally and varies with time. As `epiclccorr` should have propagated errors properly and applied the same correction factor to the count rates and errors, we can get an estimate of f in every time bin with the following equation,

$$f = \text{err}(x(t)) / \sqrt{\frac{s(t) + b(t)}{\Delta t}} \quad (\text{A7})$$

where $x(t)$ is the flux-corrected light curve produced by the `epiclccorr` task, $s(t)$ the source light curve before background subtraction, and $b(t)$ the background light curve *rescaled* to the size of the source extraction region. Then we can derive a mean correction factor \bar{f} , and use \bar{x}/\bar{f} to replace \bar{x} in Equation A6 to get a better estimate of the true PN_{lev} . The green line in Figure A1 shows the new estimate of PN_{lev} , which is higher and more consistent with the constant white-noise power observed at high frequencies.

Another method is to measure PN_{lev} from the periodogram directly. [Timmer & Koenig \(1995\)](#) showed that the probability distribution of a periodogram at a specific frequency follows a χ^2 distribution with two degrees of freedom; thus PN_{lev} can be estimated by taking the arithmetic average of the power over the frequency range where the Poisson noise power dominates. After visually checking all the periodograms, we choose the frequency range above 2×10^{-3} Hz to measure PN_{lev} . The blue dash line in Figure A1 shows the averaged Poisson noise power, which is most consistent with the constant white-noise power observed at high frequencies. Therefore, we adopt this method to determine the true PN_{lev} , which is then used to calculate the intrinsic rms variability. It should be noted that the above method requires a proper time bin of the light curve. The binning time is mainly determined by the following two factors. Firstly, a short time bin should be used to ensure that the periodogram can show the constant Poisson noise power at high frequencies. Secondly, the time bin should not be too short, as otherwise it will create many zero-count bins in the light curve, which will bias the periodogram at high frequencies. We find that for our sample a bin size of 50-100 s is appropriate for most observations, but larger time bins must be used for very faint sources.

B. TYPICAL RESULTS OF OUR SAMPLE

Here we plot some typical results of 78 Seyfert galaxies in Figure A2 ⁶.

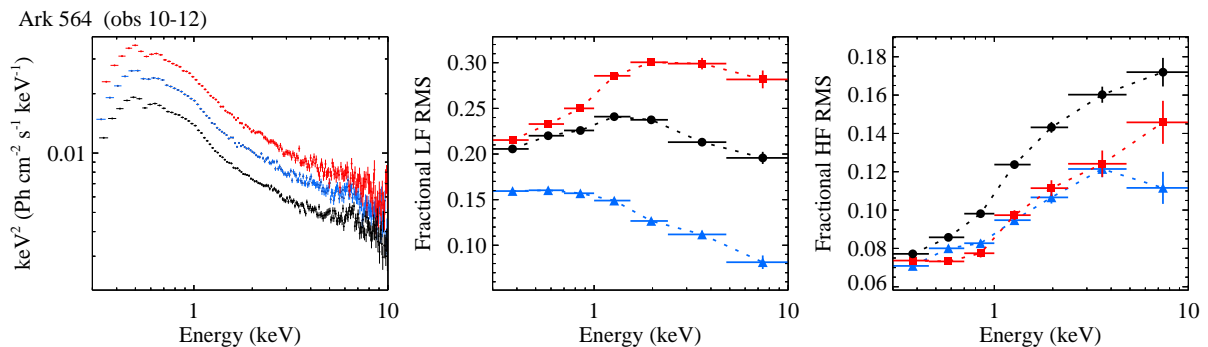


Figure A2. Connection of the rms spectrum with the time-averaged spectrum for the sample. The complete figure set (78 images) is available in the online journal. Each three observations of one source are plotted in one picture, and different colors are defined as flux states. The lowest, intermediate, and highest fluxes are shown in black, blue, and red, respectively. Displayed in black if there is only one observation, in black and red if there are two observations, but always with black as representative of the low flux and red of the high flux. The left panel shows the time-averaged energy spectra for each of the individual observations used in this source. The middle panel shows the fractional rms in LF ($< 10^{-4}$ Hz). The right panel shows the fractional rms in HF (10^{-4} - 10^{-3} Hz).

⁶ All the spectral files and images can be downloaded from our website. <https://gohujingwei.github.io/rms.html>.